

## Research Paper

## Anomalous elasticity of talc at high pressures: Implications for subduction systems

Ye Peng<sup>a,\*</sup>, Mainak Mookherjee<sup>a</sup>, Andreas Hermann<sup>b</sup>, Geeth Manthilake<sup>c</sup>, David Mainprice<sup>d</sup><sup>a</sup> Earth Materials Laboratory, Department of Earth, Ocean, and Atmospheric Sciences, Florida State University, Tallahassee, FL 32306, USA<sup>b</sup> Centre for Science at Extreme Conditions and SUPA, School of Physics and Astronomy, The University of Edinburgh, Edinburgh EH9 3FD, UK<sup>c</sup> Laboratoire Magmas et Volcans CNRS, IRD, OPGC, Université Clermont Auvergne, 63000 Clermont-Ferrand, France<sup>d</sup> Geosciences Montpellier, UMR CNRS 5243, Université de Montpellier, Montpellier 34095, France

## ARTICLE INFO

## Article history:

Received 9 September 2021

Revised 4 February 2022

Accepted 11 March 2022

Available online 15 March 2022

Handling Editor: R.D. Nance

## Keywords:

Talc

Elasticity

Seismic anisotropy

Hydrous minerals

Subduction zone

## ABSTRACT

Talc is a layered hydrous silicate mineral that plays a vital role in transporting water into Earth's interior and is crucial for explaining geophysical observations in subduction zone settings. In this study, we explored the structure, equation of state, and elasticity of both triclinic and monoclinic talc under high pressures up to 18 GPa using *first principles* simulations based on density functional theory corrected for dispersive forces. Our results indicate that principal components of the full elastic constant tensor  $C_{11}$  and  $C_{22}$ , shear components  $C_{66}$ , and several off-diagonal components show anomalous pressure dependence. This non-monotonic pressure dependence of elastic constant components is likely related to the structural changes and is often manifested in a polytypic transition from a low-pressure polytype talc-I to a high-pressure polytype talc-II. The polytypic transition of talc occurs at pressures within its thermodynamic stability. However, the bulk and shear elastic moduli show no anomalous softening. Our study also shows that talc has low velocity, extremely high anisotropy, and anomalously high  $V_p/V_s$  ratio, thus making it a potential candidate mineral phase that could readily explain unusually high  $V_p/V_s$  ratio and large shear wave splitting delays as observed from seismological studies in many subduction systems.

© 2022 China University of Geosciences (Beijing) and Peking University. Production and hosting by Elsevier B.V. This is an open access article under the CC BY-NC-ND license (<http://creativecommons.org/licenses/by-nc-nd/4.0/>).

## 1. Introduction

Water plays a vital role in the solid Earth by influencing melting processes, i.e., lowering solidus temperature (Hirschmann, 2006), facilitating mantle convection by affecting rheological properties of rocks, and affecting geophysical observations such as seismic velocities and geoelectric fields (Karato, 2008). As plates subduct, bending-related faults often lead to hydration of the oceanic lithosphere, which in turn stabilizes a suite of hydrous minerals (Ranero et al., 2003). Talc,  $Mg_3Si_4O_{10}(OH)_2$ , is one such hydrous mineral. It stores ~4.7 wt.% water locked up in its crystal structure as hydroxyl ions. It has limited thermal stability up to ~800–820 °C at ~3 GPa, i.e., 95 km. Due to its negative Clapeyron slope ( $dP/dT < 0$ ) at pressures >3 GPa, the thermal stability of talc is reduced to 710 °C at 5 GPa, i.e., 155 km (Pawley and Wood, 1995). Upon reaching adequate depths, hydrous minerals dehydrate and release aqueous fluids. The upward migration of these

aqueous fluids further stabilizes hydrous minerals such as talc and serpentine in the relatively cooler regions of the overlying mantle wedge (Evans et al., 1976). The dehydration of these hydrous minerals is often manifested as the double seismic zones (Brudzinski et al., 2007; Dorbath et al., 2008; Rondenay et al., 2008).

Talc and other hydrous minerals play an important role in transporting water into the Earth's interior. Effective transport of water through the subduction zone is achieved by the transfer of water from progressively denser hydrous mineral phases. In other words, if the geothermal gradient overlaps with the stability field of hydrous minerals, water is likely to be effectively sequestered within the hydrous minerals and dragged along with the subducting plate. Serpentine is a hydrous mineral that is thermodynamically stable up to a depth of ~200 km in a relatively cold subduction zone. As serpentine dehydrates, it often transfers water to a denser hydrous mineral phase, phase A, which is stable at a deeper depth. Often the thermodynamic stability fields of serpentine and phase A do not fully overlap, i.e., the geothermal gradient passes through a region where no hydrous mineral is stable, creating a thermodynamic choke point in the effective transport of

\* Corresponding author.

E-mail address: [yp16b@fsu.edu](mailto:yp16b@fsu.edu) (Y. Peng).

water into the deep Earth. Experimental studies have shown that at such a thermodynamic choke point, talc may intercalate water in its interlayer and stabilize the 10-Å phase that is crucial in transporting water deep down to dense hydrous mineral phases (Pawley and Wood, 1995; Pawley et al., 1995; Ohtani et al., 2004; Gleason et al., 2008; Rashchenko et al., 2016). The 10-Å phase is a layered hydrous silicate mineral with crystal structure similar to that of talc. It is argued that the formation of 10-Å phase might be facilitated at pressures where talc is observed to undergo polytypic transitions (Gleason et al., 2008; Rashchenko et al., 2016).

Talc is a layered hydrous silicate mineral with a crystal structure that consists of an octahedral (O) layer sandwiched by two tetrahedral (T) layers (TOT), i.e., three  $\text{MgO}_6$  octahedral units are sandwiched between two  $[\text{Si}_2\text{O}_5]^{2-}$  units such that their apical oxygen atoms are pointing towards each other. The two hydroxyls ( $\text{OH}^-$ ) attached to the  $\text{MgO}_6$  octahedra point within the di-trigonal rings formed by the tetrahedral units and are perpendicular to the (001) plane. The adjacent TOT layers are held by weak van der Waals (vdW) forces. Due to the layered crystal structure, talc is one of the softest minerals with a Mohs hardness scale of 1 (Wenk and Bulakh, 2016) and has a very low coefficient of friction  $\sim 0.16$ – $0.23$  at room temperature (Escartín et al., 2008; Moore and Lockner, 2008). Talc is often resistant to slip when the rate of sliding is faster (Moore and Lockner, 2008). These characteristics make talc an ideal lubricant to allow slow and stable sliding/creeping along the subduction interface, inhibiting the elastic energy build-up and preventing fast sliding and unstable slip related to large earthquakes (Wibberley, 2007).

Talc is a common mineral and is often found in metamorphosed or hydrothermally altered lithologies. Because of its widespread occurrence, stability, and unique physical properties, the presence of talc is often invoked to explain anomalous geophysical observations. For example, it is suggested that talc might explain observations along many oceanic faults that occur in slow and ultra-slow spreading mid-ocean ridges (Schroeder and John, 2004; Boschi et al., 2006) and stable fast creeping sections of the San Andreas fault (Moore and Rymer, 2007; Wibberley, 2007). It is proposed that a talc-rich mélange zone forms in the slab-mantle interface and contributes to the low-velocity zone observed at or above the slab surface (Bebout and Barton, 2002; Spandler et al., 2008; Marschall and Schumacher, 2012). The stable-sliding behavior of talc leads to aseismicity and therefore controls the maximum depth of earthquakes in subduction zones (Peacock and Hyndman, 1999). It is also suggested that talc may promote slow-slip earthquakes, i.e., an earthquake-like event that releases comparable energies with a much slower rate, five-order slower, than those of ordinary great earthquakes (Kawasaki, 2004; Mainprice et al., 2008). In the central Mexican subduction zone, a thin layer at the top of the slab, which is characterized by ultra-slow velocity, low viscosity, high P-to-S velocity ratio ( $V_P/V_S$ ), and free of earthquakes, has also been linked to the presence of talc (Kim et al., 2013). In the flat subduction system of central Mexico, talc is also suggested to play an important role in the dynamic process of slab-flattening (Manea and Gurnis, 2007; Kim et al., 2013).

Despite the importance of talc in subduction zone settings, little is known about its elasticity. Owing to the difficulty in finding good quality single crystals, experimental data on full elastic constants are currently lacking. Attempts have been made to estimate the shear modulus from ultrasonic compressional sound wave velocity (Bailey and Holloway, 2000); however, so far, no known Brillouin scattering result exists for talc. In contrast to the full elastic constant tensor, a significant amount of experimental studies has provided constraints on the bulk modulus from the studies of the equation of state (Pawley et al., 2002; Gleason et al., 2008; Gatta et al., 2013).

So far, the equation of state and elasticity of talc have been explored by at least three prior *first principles* simulation studies (Stixrude, 2002; Mainprice et al., 2008; Ulian et al., 2014). The equation of state study using *first principles* explored the high pressure evolution of the crystal structure and linear compressibility of triclinic talc but did not explore the full elastic constant tensor (Stixrude, 2002). This was followed by a study that determined the full elastic constant tensor and elastic anisotropy of both monoclinic and triclinic talc up to 12 GPa (Mainprice et al., 2008). However, since talc is a layered hydrous silicate, the vdW interactions often play a vital role, and relevant correction is needed to better describe its structure and elastic properties (Weck et al., 2015). In addition, the predicted pressure dependence of the elastic constants and elastic moduli for the triclinic and monoclinic polymorphs were quite different, and the pressure dependence also indicated a significant scattering due to poorly converged energetics. More recent work on talc explored the structure and elastic properties using *first principles* simulation integrated with dispersive forces contribution (Ulian et al., 2014). However, the full elastic constant results were limited to ambient pressure. It is well known that pressure significantly influences the elasticity of layered hydrous minerals. Hence, in this study, we explored the structure, equation of state, and elasticity of both triclinic and monoclinic talc using *first principles* simulations incorporating dispersive interaction corrections at high pressures up to 18 GPa.

## 2. Methods

In nature, talc ( $\text{Mg}_3\text{Si}_4\text{O}_{10}(\text{OH})_2$ ) is reported to crystallize in either monoclinic space group symmetry (C2/c) with two TOT layers ( $Z = 4$ ) (Gruner, 1934) or triclinic space group symmetry (C1) (Rayner and Brown, 1973; Perdikatsis and Burzlaff, 1981) with one TOT unit ( $Z = 2$ ). Hence, in this study, we explored both triclinic and monoclinic polymorphs. We explored the high-pressure behavior of crystal structure, equation of state, and elasticity of talc using static density functional theory as implemented in the Vienna ab-initio simulation package (VASP) (Hohenberg and Kohn, 1964; Kohn and Sham, 1965; Kresse and Hafner, 1993; Kresse and Furthmüller, 1996a,b; Kresse and Joubert, 1999). *First principles* simulations based on density functional theory are crucial in providing valuable insights into the energetics, structure, and elasticity of hydrous minerals (Tsuchiya et al., 2005; Tsuchiya and Tsuchiya, 2009, 2011; Chantel et al., 2012; Ulian et al., 2014; Mookherjee et al., 2015, 2016, 2019; Mookherjee and Tsuchiya, 2015; Peng et al., 2017; Yang et al., 2017; Ulian and Valdrè, 2017, 2019; Peng and Mookherjee, 2020; Lee et al., 2021; Saha et al., 2021). We used generalized gradient approximation (GGA) (Perdew et al., 1996) and the highly accurate projector augmented wave method (PAW) implemented in VASP (Kresse and Joubert, 1999).

It is well known that dispersive interaction corrections often provide better prediction of the structure and properties of layered minerals (Ulian et al., 2014; Weck et al., 2015). Hence, to account for the long-range dispersive interactions, we computed the equation of state and elasticity of talc with optB88 vdW density functional as implemented in VASP (Dion et al., 2004; Klimeš et al., 2009, 2011; Román-Pérez and Soler, 2009).

We performed a series of convergence tests on talc by varying the cutoff energy and  $k$ -points. Unlike the previous study where a low cutoff energy  $E_{\text{cut}}$  of 400 eV was used (Mainprice et al., 2008), we found that a cutoff energy  $E_{\text{cut}} = 900$  eV was required to describe the ground state energy of talc adequately (Supplementary Data Table 1). Similarly, we found that it needed a  $k$ -point mesh of  $6 \times 3 \times 3$  Monkhorst-Pack grid with 27 irreducible  $k$ -points (Monkhorst and Pack, 1976) (Supplementary Data Table 2).

We determined the elastic constants by straining the lattice parameters by  $\pm 1\%$ , as outlined in previous studies (Mookherjee and Stixrude, 2009; Mookherjee and Capitani, 2011; Chheda et al., 2014; Peng et al., 2017; Peng and Mookherjee, 2020). Next, we computed the compressional and shear wave velocities  $V_p(\mathbf{n})$  and  $V_s(\mathbf{n})$  as a function of propagation direction  $\mathbf{n}$  (Mainprice, 1990). The P-wave anisotropy ( $AV_p$ ) is defined as  $AV_p = (V_{pmax} - V_{pmin}) / [(V_{pmax} + V_{pmin}) / 2] \times 100\%$ . In an anisotropic media, the shear wave splits into two waves. We denoted the fastest and slowest wave as  $V_{s1}$  and  $V_{s2}$ , respectively. We calculated the shear wave polarization anisotropy ( $AV_s$ ) along each direction by  $AV_s = (V_{s1} - V_{s2}) / [(V_{s1} + V_{s2}) / 2] \times 100\%$ .

### 3. Results

#### 3.1. Equation of state and crystal structure

The energy-volume and pressure-volume behavior of talc can be well described by the 4<sup>th</sup>-order Birch-Murnaghan equation of state (EoS) (Murnaghan, 1937; Birch, 1978; Katsura and Tange,

2019) (Fig. 1). To better compare with prior EoS studies, we also fitted our data with Murnaghan EoS and 3<sup>rd</sup>-order Birch-Murnaghan EoS (Table 1). Our predicted zero-pressure volume for triclinic and monoclinic talc is  $V_0^{tri} = 461.8 \pm 0.1 \text{ \AA}^3$  and  $V_0^{mon} = 923.4 \pm 0.1 \text{ \AA}^3$ , respectively (Table 1). Experimental studies reported that the zero-pressure volume of triclinic talc is  $453.6 \pm 0.4 \text{ \AA}^3$  (Gleason et al., 2008) and  $454.7 \pm 0.9 \text{ \AA}^3$  (Gatta et al., 2013), while that of monoclinic talc is  $912 \pm 2 \text{ \AA}^3$  (Pawley et al., 2002) and  $915 \pm 8 \text{ \AA}^3$  (Gleason et al., 2008). Our results are  $\sim 1\%$ - $2\%$  larger than the experimental results. We noted that the conventional GGA tends to underestimate the binding energy and thus overestimate the volume, while the conventional local density approximation (LDA) is the opposite. But the prediction with the vdW correction showed a much better agreement with the experimental results (Supplementary Data Fig. 1). The 4<sup>th</sup>-order Birch-Murnaghan EoS fitting also yields the zero-pressure bulk modulus  $K_0^{tri} = 38.5 \pm 3 \text{ GPa}$  and the pressure derivative of the bulk modulus  $K_0'^{tri} = 13.2 \pm 0.1$  and  $K_0''^{tri} = -4.3 \pm 0.1 \text{ GPa}^{-1}$  for triclinic talc, and  $K_0^{mon} = 40.0 \pm 0.2 \text{ GPa}$  with  $K_0'^{mon} = 12.2 \pm 0.3$  and  $K_0''^{mon} = -3.6 \pm 0.3 \text{ GPa}^{-1}$  for monoclinic talc (Table 1). Our analysis

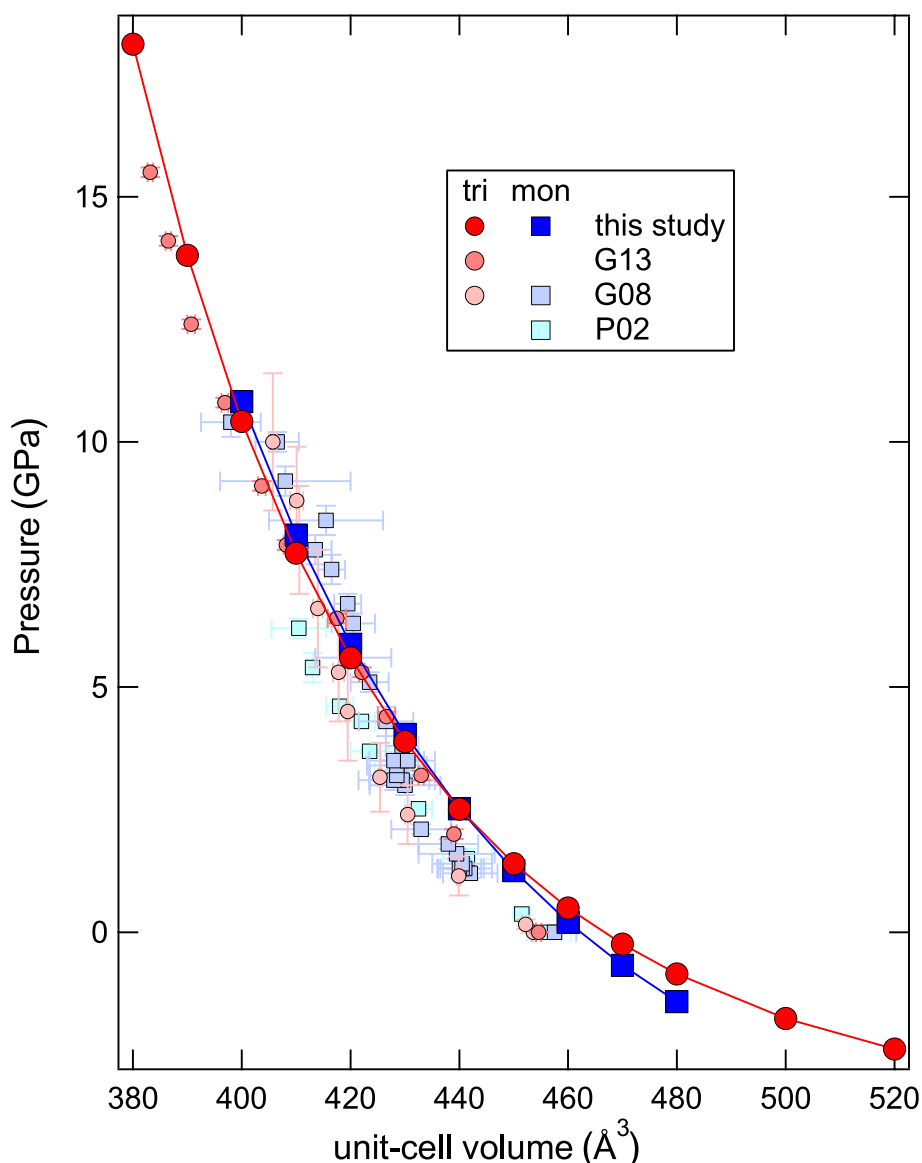


Fig. 1. Comparison between experimental results and our predicted pressure vs. unit-cell volume for triclinic (tri) and monoclinic (mon) talc. Please note that the unit-cell volume of monoclinic talc has been divided by two to compare with that of triclinic talc. G13: Gatta et al., 2013; G08: Gleason et al., 2008; P02: Pawley et al., 2002.

**Table 1**

Equation of state parameters for talc compared with previous studies. Number in the parenthesis is the error in the last digit.

	Symmetry <sup>a</sup>	Pressure range (GPa)	$E_0$ (eV)	$V_0$ (Å <sup>3</sup> )	$K_0$ (GPa)	$K'$	$K''$ (GPa <sup>-1</sup> )	EoS fitting <sup>b</sup>	Methods <sup>c</sup>
Gatta et al., 2013	tri	0–15.5		454.7(9)	57(3)	4.9(5)		M	SCND + SCXRD
	tri	0–15.5		454.7(10)	56(3)	5.4(7)		III-BM	SCND + SCXRD
Pawley et al., 2002	mon	0–6.2		912(2)	41(4)	6(2)		M	SEDXRPD
Pawley et al., 1995	mon	0–6.05		902.7(2)	41.6(9)	6.5(4)		M	XRPD
Gleason et al., 2008	tri	0–10.0		453.6(4)	30(17)	18(27)		III-BM	XRPD
	mon	0–10.4		915(8)	44(2)	18(1)		III-BM	XRPD
Stixrude, 2002	tri/primitive cell	–1.10–26.07		217.5(1)	37.8(4)	13.6(2)	–4.0	IV-BM	LDA static
	tri/primitive cell	–1.10–26.07		221.8(2)	29(5)	17	–8.6	IV-BM	LDA 300 K
Mainprice et al., 2008	tri	0–11.60		452.0	32.1	17.4	–9.1	IV-BM	GGA PAW
	mon	0–12.52		913.2	34.3	11.5	–3.0	IV-BM	GGA PAW
Ulian et al., 2014	tri	–2.2–10.0		450.34	56.25	5.66		III-BM	B3LYP-D*
This study <sup>d</sup>	tri	–2.4–18.1	–231.76(2)	466.5(8)	33(2)	8.3(6)		M	GGA PAW + vdW
	mon	–1.4–10.8	–463.518(5)	924.4(5)	43(1)	7.2(3)		M	GGA PAW + vdW
This study <sup>d</sup>	tri	–2.4–18.1	–231.75(1)	464.7(6)	34(1)	10.7(7)		III-BM	GGA PAW + vdW
	mon	–1.4–10.8	–463.514(4)	924.2(4)	41.8(9)	8.4(4)		III-BM	GGA PAW + vdW
This study <sup>d</sup>	tri	–2.4–18.1	–231.755(2)	461.8(1)	38.5(3)	13.2(1)	–4.3(1)	IV-BM	GGA PAW + vdW
	mon	–1.4–10.8	–463.510(1)	923.44(8)	40.0(2)	12.2(3)	–3.6(3)	IV-BM	GGA PAW + vdW

Note:

<sup>a</sup> : tri: triclinic; mon: monoclinic.<sup>b</sup> : M: Murnaghan fitting; III-BM: 3<sup>rd</sup>-order Birch-Murnaghan fitting; IV-BM: 4<sup>th</sup>-order Birch-Murnaghan fitting.<sup>c</sup> : SCND: single-crystal neutron diffraction; SCXRD: single-crystal X-ray diffraction; SED: synchrotron energy-dispersive; XRPD: X-ray powder diffraction; LDA: local density approximation; GGA: generalized gradient approximation; PAW: projector augmented wave; B3LYP-D\*: a hybrid exchange functional with the dispersive force correction; vdW: van der Waals correction.<sup>d</sup> : Results from this study have been fitted by Murnaghan fitting, 3<sup>rd</sup>-order Birch-Murnaghan fitting, and 4<sup>th</sup>-order Birch-Murnaghan fitting. The  $\chi^2$  of triclinic and monoclinic talc are 1.1E-2 and 3.9E-4 using Murnaghan fitting, 5.0E-3 and 2.2E-4 using 3<sup>rd</sup>-order Birch-Murnaghan fitting, 8.6E-5 and 4.3E-6 using 4<sup>th</sup>-order Birch-Murnaghan fitting, respectively.

indicates that different types of EoS fitting affect the fitting results significantly. In addition, there is also a strong correlation between  $K_0$  and  $K'_0$  which is known for other minerals. Such a correlation means that the energy-volume data can be fitted equally well by varying the value of  $K_0$  and  $K'_0$ . This must be considered when comparing a set of EoS parameters with previous results (Angel, 2000).

The lattice parameters of talc decrease with pressures for both triclinic and monoclinic structures (Fig. 2). However, the change in the  $c$ -axis is much more considerable compared with the  $a$ - and  $b$ -axis. We used  $f_i$ - $F_i$  relations to determine the linear incompressibility along each axis, where  $f_i$  is linear finite strain and  $F_i$  is the linear normalized pressure (the subscript “ $i$ ” represents each axis) (Davies, 1974; Weaver, 1976; Meade and Jeanloz, 1990; Wentzcovitch and Stixrude, 1997; Chheda et al., 2014). Both triclinic and monoclinic talc show the relation of  $K_a \sim K_b \gg K_c$ , indicating a large anisotropy in the linear compressibility (Supplementary Data Table 3, Fig. 2). Upon compression, the volume and average bond distance of each polyhedral unit decrease (Supplementary Data Fig. 2). The hydroxyl bond distance slightly increases upon compression, and beyond 1.4 GPa, it decreases monotonously with pressure. The tetrahedral rotation angle  $\theta = (\sum_{i=1}^6 |\phi_i - 120^\circ|)/12$  captures the degree of distortion in the six-membered tetrahedral rings, where  $\phi_i$  is the angle among three adjacent basal oxygen atoms. Our results show that the tetrahedral rotation angle  $\theta$  increases upon compression consistent with prior experimental studies (Perdikatsis and Burzlaff, 1981; Gatta et al., 2013) (Supplementary Data Fig. 2).

### 3.2. Elasticity

To determine the elasticity of talc, we considered both triclinic and monoclinic polymorphs. The talc crystal with triclinic symmetry has 21 independent elastic constants, while the talc crystal with monoclinic symmetry has 13 independent ones (Nye, 1985). In the pressure range explored in this study, the principal components of elastic constant exhibit the following relation of  $C_{11} \sim C_{22} > C_{33}$  (Figs. 3 and 4, Tables 2 and 3).

Upon compression, the principal components  $C_{11}$  and  $C_{22}$  soften up to pressures of 3 GPa. Upon further compression beyond 3 GPa,  $C_{11}$  and  $C_{22}$  stiffen. In contrast to  $C_{11}$  and  $C_{22}$ , the  $C_{33}$  increases monotonously. We also noted that  $C_{12}$ ,  $C_{15}$ ,  $C_{25}$ ,  $C_{36}$ , and  $C_{45}$  of triclinic talc and  $C_{12}$  of monoclinic talc show initial softening till  $\sim 3$  GPa, following which they show normal pressure dependence. While  $C_{66}$  and  $C_{14}$  of triclinic talc and  $C_{66}$  of monoclinic talc all exhibit opposite pressure dependence, i.e., they first stiffen up to 3 GPa and then soften upon compression (Figs. 3 and 4). The transition occurs within the thermodynamic stability of talc and is observed in both triclinic and monoclinic polymorphs. It is a rather unique behavior and is likely related to the reported polytypic transition between the low-pressure polytype talc-I to the high-pressure polytype talc-II (Scott et al., 2007; Gleason et al., 2008). This transition is related to the shearing between the weakly bonded adjacent TOT layers along the  $a$ - $b$  plane, i.e., the change of the stacking angle of TOT layers. The shearing is likely to facilitate the water intercalation into talc and thus the formation of the 10-Å phase (Gleason et al., 2008). Owing to such shearing between the adjacent TOT layers,  $C_{ij}$ s with stresses acting along the  $a$ - and  $b$ -directions, i.e., subscripts of 1, 2, and 6, tend to be more sensitive and hence show anomalous pressure dependence.

The polytypic transition is often characterized by pressure-induced structural adjustments, resulting in iso-symmetric changes in the stacking sequences of the tetrahedral and octahedral layers. In addition to talc, similar transitions have been observed in several layered hydrous silicates relevant to subduction zones, including kaolinite (Welch and Crichton, 2010; Basu and Mookherjee, 2021), chlorite (Welch et al., 2004), and serpentine (Nestola et al., 2010). Such transitions are often associated with the pressure-induced anomalies of elastic constants. For instance, prior *first principles* predictions of serpentine polymorphs-lizardite (Mookherjee and Stixrude, 2009; Tsuchiya, 2013) and antigorite (Mookherjee and Capitani, 2011), and chlorite (Mookherjee and Mainprice, 2014) reported anomalous elasticity under compression. Experimental studies on the pressure dependence of elastic constants are often rare, except for one Brillouin scattering study of antigorite, which also revealed the pressure-

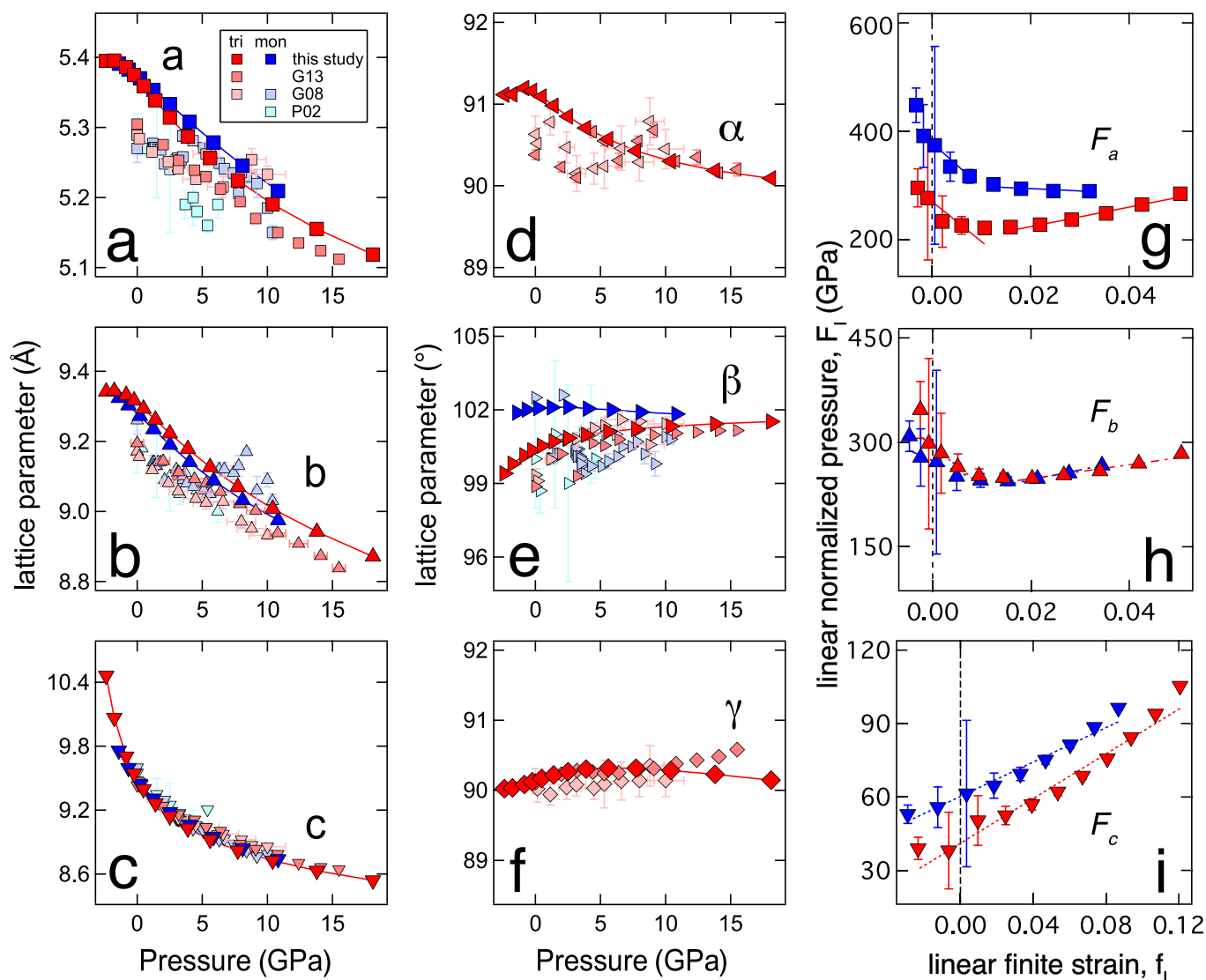


**Fig. 2.** (a–c) Lattice parameters (a) *a*-, (b) *b*-, (c) *c*-axis of talc as a function of pressure. Please note that the *c*-axis of monoclinic talc has been divided by two to compare with that of triclinic talc. (d–f) Angular lattice parameters (d)  $\alpha$ , (e)  $\beta$ , (f)  $\gamma$  as a function of pressure. Our predicted results are compared with experimental results of talc (G13: Gatta et al., 2013; G08: Gleason et al., 2008; P02: Pawley et al., 2002). (g–i) The linear normalized pressure,  $F_i$ , vs. the linear Eulerian finite strain,  $f_i$ , is plotted for (g) *a*-, (h) *b*-, (i) *c*-axis. The intercept along the ordinate indicates the linear compressibility  $K_a$ ,  $K_b$ , and  $K_c$ . The error bars for the normalized pressure are estimated to be  $\pm 0.1$  GPa based on the numerical precision of the calculations determined from the convergence of the energy.

induced anomaly (Bezacier et al., 2013). Hence, such transitions are often manifested in the changes in the pressure–volume relations and high-pressure vibrational spectroscopy, as documented in serpentine polymorphs antigorite (Nestola et al., 2010) and lizardite (Auzende et al., 2004), chlorite (Welch et al., 2004), kaolinite (Welch and Crichton, 2010; Basu and Mookherjee, 2021), and dickite (Johnston et al., 2002; Dera et al., 2003).

At pressures beyond the anomalous behavior, the rate of stiffening of  $C_{11}$  and  $C_{22}$ , i.e., the pressure dependence  $dC_{ii}/dP$ , where  $i = 1$  or 2, is significantly lower than that of  $C_{33}$ , i.e.,  $dC_{33}/dP$ . Similar behavior has been often observed in other layered hydrous silicates, including serpentine polymorph lizardite (Mookherjee and Stixrude, 2009; Tsuchiya, 2013), antigorite (Mookherjee and Capitani, 2011; Bezacier et al., 2013), chlorite (Mookherjee and Mainprice, 2014), and phlogopite (Chheda et al., 2014). We noticed that the pressure dependence of  $C_{13}$  and  $C_{23}$  is much larger than that of  $C_{12}$ , and similarly, the pressure dependence of  $C_{44}$  and  $C_{55}$  is much larger than that of  $C_{66}$  for the entire pressure range explored in this study.

The comparison of elastic constants between our study and prior estimates showed significant differences in  $C_{ij}$ s (Figs. 3 and 4) (Mainprice et al., 2008). These differences are likely due to both the dispersive interaction correction and the high cutoff energy (900 eV) used in this study. In contrast, the previous study did not use any correction for the dispersive force and used much lower cutoff energy (400 eV). Owing to the low cutoff energy and very likely non-converged results, prior results exhibited scattered data of elasticity versus pressure (Mainprice et al., 2008). However, there is a qualitative agreement between the prior study and our work in the talc-I to talc-II transition, and both capture the change in pressure dependence of elastic constants.

We determined the Hill averages of bulk and shear moduli based on Voigt and Reuss bounds (Fig. 5). The zero-pressure bulk and shear moduli are in good agreement with previous experimental studies (Babeyko et al., 1994; Bailey and Holloway, 2000). Our results show that the elastic moduli of talc increase with pressure. In addition, the results of triclinic and monoclinic talc crystal match very well, indicating that the symmetry has almost no effect

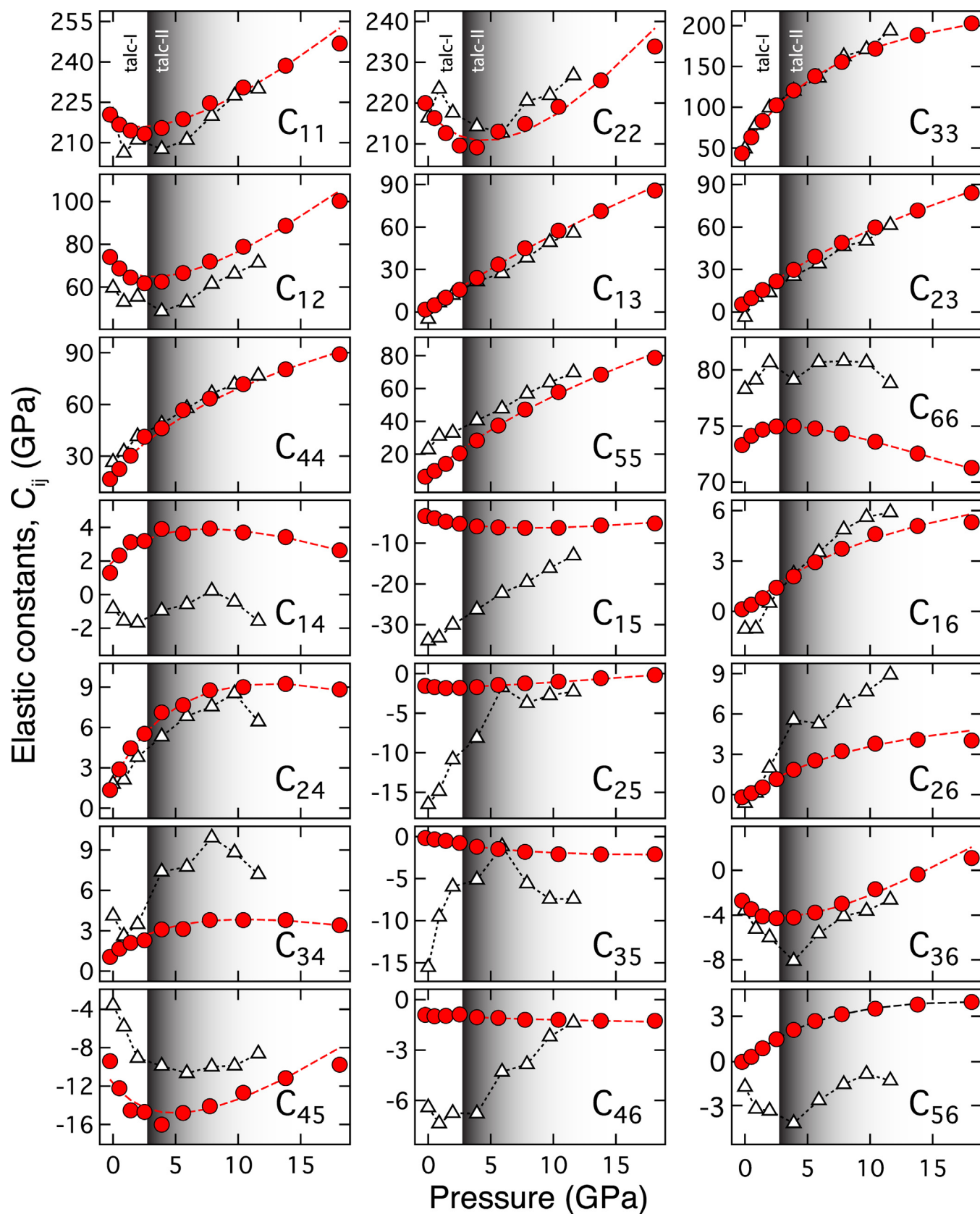


**Fig. 3.** Elastic constants  $C_{ij}$  of triclinic talc as a function of pressure. Triclinic talc has 21 independent elastic constants, and each panel has been labeled. The gray shaded area marks talc-I to talc-II transition. Our results are compared with previous simulation results (black triangles) (Mainprice et al., 2008).

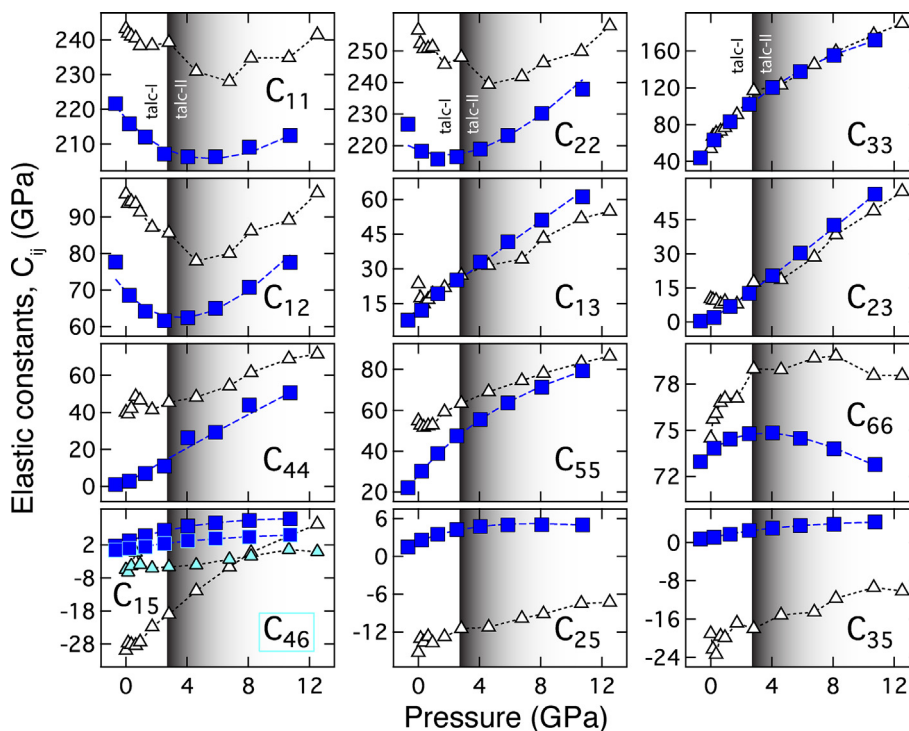


**Fig. 4.** Elastic constants  $C_{ij}$  of monoclinic talc as a function of pressure. Monoclinic talc has 13 independent elastic constants, and each panel has been labeled. The gray shaded area marks talc-I to talc-II transition. Our results are compared with previous simulation results (black triangles) (Mainprice et al., 2008).

**Table 2**  
Elastic constants for triclinic talc.

V	P	C <sub>11</sub>	C <sub>12</sub>	C <sub>13</sub>	C <sub>14</sub>	C <sub>15</sub>	C <sub>16</sub>	C <sub>22</sub>	C <sub>23</sub>	C <sub>24</sub>	C <sub>25</sub>	C <sub>26</sub>	C <sub>33</sub>	C <sub>34</sub>	C <sub>35</sub>	C <sub>36</sub>	C <sub>44</sub>	C <sub>45</sub>	C <sub>46</sub>	C <sub>55</sub>	C <sub>56</sub>	C <sub>66</sub>	K <sub>H</sub>	G <sub>H</sub>
(Å <sup>3</sup> )		(GPa)																						
470	-0.2	220.4	74.1	1.8	1.3	-3.3	0.1	220.0	5.3	1.4	-1.5	-0.2	43.4	1.1	-0.2	-2.7	16.7	-9.4	-0.9	6.2	0.0	73.3	53.2	24.6
460	0.5	216.7	68.7	4.8	2.3	-3.9	0.4	216.3	9.7	2.9	-1.7	0.1	63.1	1.7	-0.3	-3.5	22.6	-12.2	-1.0	9.8	0.3	74.1	60.1	29.3
450	1.4	214.5	64.5	10.1	3.1	-4.7	0.8	212.6	15.5	4.5	-1.8	0.5	83.2	2.1	-0.5	-4.1	30.2	-14.5	-1.0	14.1	0.9	74.7	67.2	35.6
440	2.5	213.3	61.7	15.7	3.2	-5.3	1.4	209.6	21.7	5.5	-1.8	1.2	102.3	2.3	-0.8	-4.3	41.2	-14.7	-0.9	20.5	1.5	75.0	73.8	45.3
430	3.9	215.4	62.5	24.1	3.9	-5.9	2.1	209.1	29.7	7.1	-1.7	1.9	120.7	3.1	-1.2	-4.2	46.2	-16.0	-1.0	28.3	2.1	75.0	81.8	51.1
420	5.6	218.8	66.6	33.5	3.6	-6.1	2.9	213.0	39.1	7.7	-1.4	2.6	138.1	3.1	-1.5	-3.8	56.8	-14.8	-1.1	37.5	2.7	74.8	90.9	58.4
410	7.7	224.7	71.9	45.0	3.9	-6.3	3.7	214.9	49.0	8.8	-1.2	3.2	155.4	3.8	-1.8	-3.0	63.4	-14.1	-1.2	47.3	3.1	74.3	100.6	63.3
400	10.4	230.5	78.9	57.4	3.7	-6.2	4.6	219.1	59.7	9.0	-1.0	3.8	171.8	3.8	-2.1	-1.7	71.8	-12.7	-1.2	57.9	3.5	73.6	110.9	67.8
390	13.8	238.6	88.8	71.2	3.4	-5.7	5.1	225.6	71.7	9.2	-0.6	4.1	188.3	3.8	-2.1	-0.4	80.4	-11.2	-1.3	68.5	3.8	72.5	122.7	71.6
380	18.1	246.8	100.3	85.8	2.6	-5.1	5.3	233.9	84.1	8.8	-0.2	4.0	202.8	3.4	-2.1	1.1	89.1	-9.8	-1.3	78.7	4.0	71.3	134.9	74.6
<i>finite strain fit</i>																								
466.5	C <sub>ij0</sub>	217.3	70.6	1.6	2.0	-3.6	0.0	218.0	6.1	2.0	-1.7	-0.2	51.4	1.2	-0.1	-3.2	20.0	-11.7	-0.9	6.3	-0.1	73.7	58.0	26.9
	C <sub>ij</sub> '	-1.5	-4.4	6.6	0.7	-1.0	0.8	-3.9	7.7	1.9	-0.0	0.7	25.2	0.8	-0.4	-0.7	8.5	-1.7	-0.1	7.3	0.8	0.9	6.5	6.3
	C <sub>ij</sub> ''	0.9	2.2	-0.4	-0.3	0.3	-0.1	1.4	-1.0	-0.6	0.1	-0.2	-5.9	-0.2	0.1	0.4	-1.5	0.7	0.0	-0.9	-0.2	-0.6	-0.2	-0.4

Note: C<sub>ij0</sub> is the C<sub>ij</sub> at zero pressure in the unit of GPa, C<sub>ij</sub>' is the pressure derivative of C<sub>ij</sub> which is unitless, and C<sub>ij</sub>'' is the second order pressure derivative of C<sub>ij</sub> in the unit of

on the elastic properties of talc. At 0 GPa, the bulk and shear moduli of triclinic talc crystal are 58.0 and 26.9 GPa, respectively (Table 2). While the bulk and shear moduli of monoclinic talc crystal are 58.9 and 29.6 GPa, respectively (Table 3). The predicted P- and S-wave velocities of talc also increase with pressure. Similarly, the symmetry has almost no effect on the velocity of talc. At 0 GPa, the V<sub>P</sub> and V<sub>S</sub> of triclinic talc are respectively 6.0 and 3.2 km/s at a density of 2.70 g/cm<sup>3</sup>. For monoclinic talc, the V<sub>P</sub> and V<sub>S</sub> are 6.0 and 3.3 km/s with a density of 2.72 g/cm<sup>3</sup>.

Prior simulation results show a scattering in the pressure dependence (Mainprice et al., 2008). In addition, the shear modulus and velocities predicted in earlier studies show significant divergence between the different symmetries (Mainprice et al., 2008) and are significantly higher than our current results (Mainprice et al., 2008; Ulian et al., 2014) (Fig. 5). Again, the scat-

tering in the pressure dependence of the elasticity data of the prior study is likely due to the lower cutoff energy and non-converged results.

## 4. Discussion

### 4.1. Anisotropy

It is well known that talc is an extremely anisotropic mineral, as evident from its structure and resulting elastic properties. It is also known to develop a strong crystallographic preferred orientation along interfaces of thrust faults and between subduction slab and mantle wedge (Lee et al., 2020; Nagaya et al., 2020). Thus, we determined the seismic wave velocities V<sub>P</sub>, V<sub>S1</sub>, and V<sub>S2</sub> along different propagation directions (Supplementary Data Figs. 3–8). At

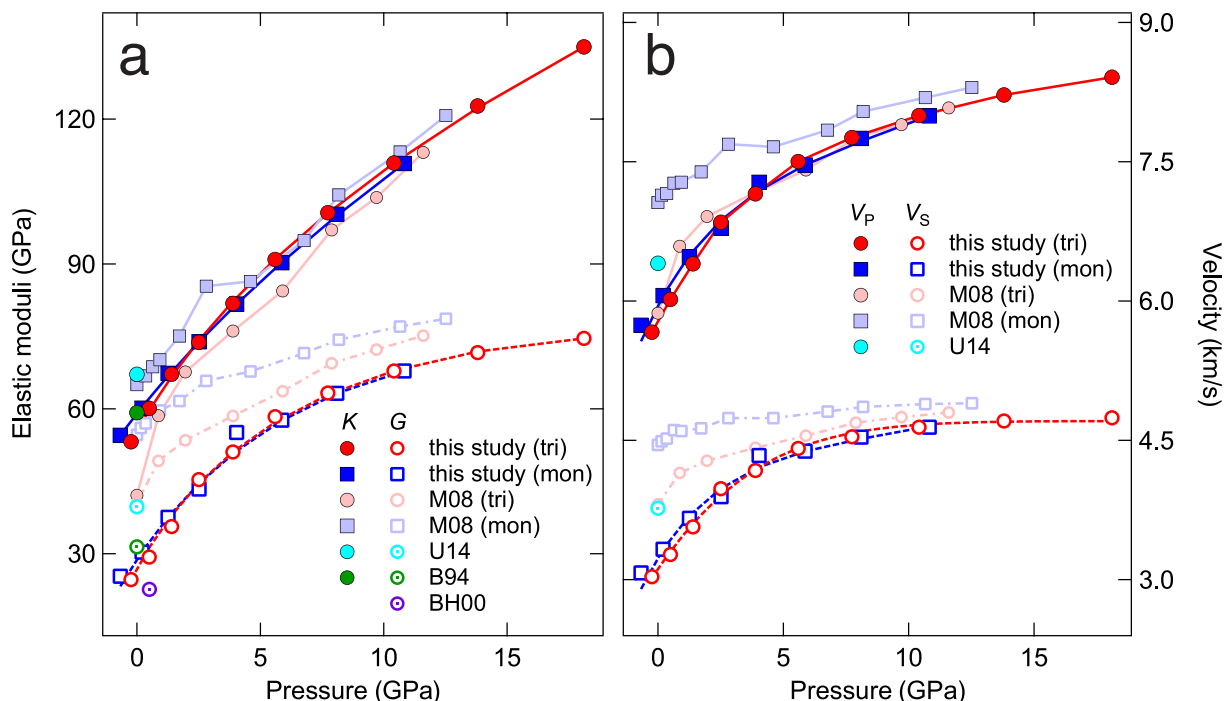


**Fig. 5.** (a) Voigt-Reuss-Hill averaging bulk ( $K$ ) and shear ( $G$ ) moduli of talc as functions of pressure. The solid symbols represent bulk moduli, while the hollow symbols represent shear moduli. The circle symbols denote triclinic talc, while the square symbols denote monoclinic talc. The results are compared with previous simulation studies (M08: Mainprice et al., 2008; U14: Ulian et al., 2014) and experimental studies (B94: Babeyko et al., 1994; BH00: Bailey and Holloway, 2000). (b) Compressional ( $V_P$ ) and shear ( $V_S$ ) wave velocity of talc as a function of pressure. The solid symbols represent compressional wave velocity, while the hollow symbols represent shear wave velocity. The circle symbols denote triclinic talc, while the square symbols denote monoclinic talc. The results are compared with previous simulation studies (M08: Mainprice et al., 2008; U14: Ulian et al., 2014).

**Table 3**  
Elastic constants for monoclinic talc.

$V$	$P$	$C_{11}$	$C_{12}$	$C_{13}$	$C_{15}$	$C_{22}$	$C_{23}$	$C_{25}$	$C_{33}$	$C_{35}$	$C_{44}$	$C_{46}$	$C_{55}$	$C_{66}$	$K_H$	$G_H$
( $\text{\AA}^3$ )		(GPa)														
940	-0.7	221.7	77.7	7.8	1.7	226.8	0.4	1.5	43.7	0.7	1.0	0.4	22.1	73.0	54.5	23.2
920	0.2	215.8	68.5	12.1	3.2	218.1	2.1	2.6	63.4	1.1	2.9	0.9	30.3	73.8	60.4	30.3
900	1.3	212.0	64.2	19.3	4.8	215.7	7.0	3.5	83.2	1.7	6.9	1.5	38.8	74.4	66.8	37.5
880	2.5	207.1	61.6	25.1	6.5	216.5	12.6	4.2	102.1	2.5	11.0	2.4	47.5	74.8	73.9	44.6
860	4.0	206.3	62.4	32.9	7.7	218.9	20.4	4.7	120.4	3.0	26.3	3.3	55.5	74.8	81.7	51.3
840	5.9	206.3	65.0	41.7	8.7	223.2	30.4	5.0	137.8	3.5	29.3	4.0	63.6	74.5	90.3	57.6
820	8.1	209.0	70.7	51.1	9.5	230.2	42.6	5.0	155.2	3.8	43.9	4.4	71.3	73.8	100.0	63.2
800	10.7	212.5	77.6	61.2	9.9	237.9	56.2	5.0	171.9	4.3	50.6	5.1	79.3	72.8	110.8	67.8
<i>finite strain fit</i>																
924.4	$C_{ij0}$	217.3	69.5	12.4	2.9	218.5	1.1	2.4	59.1	1.1	1.8	0.7	28.4	73.7	58.9	29.6
	$C'_{ij}$	-4.9	-4.6	4.9	1.7	-1.9	4.3	0.9	20.2	0.7	4.9	0.8	8.8	0.8	6.2	6.2
	$C''_{ij}$	1.4	1.8	-0.0	-0.4	1.2	0.3	-0.2	-3.3	-0.1	-0.1	-0.1	-1.4	-0.4	-0.3	-0.5

Note:  $C_{ij0}$  is the  $C_{ij}$  at zero pressure in the unit of GPa,  $C'_{ij}$  is the pressure derivative of  $C_{ij}$  which is unitless, and  $C''_{ij}$  is the second order pressure derivative of  $C_{ij}$  in the unit of

ambient conditions, the single-crystal anisotropy of talc is  $AV_P^{tri} \sim 68\%$ ,  $AV_S^{tri} \sim 150\%$ ,  $AV_P^{mon} \sim 69\%$ , and  $AV_S^{mon} \sim 141\%$  (Fig. 6). Upon compression, both  $AV_P$  and  $AV_S$  decrease significantly. When the pressure increases to  $\sim 6$  GPa, the anisotropy is almost converged with  $AV_P^{tri} \sim 29\%$ ,  $AV_S^{tri} \sim 43\%$ ,  $AV_P^{mon} \sim 28\%$ , and  $AV_S^{mon} \sim 39\%$ . Compared with other layered hydrous silicates, including chlorite (Mookherjee and Mainprice, 2014) and antigorite serpentine (Mookherjee and Capitani, 2011), talc has the largest anisotropy at low pressures. Especially,  $AV_S$  is almost three times larger than that of chlorite and antigorite. However, previous work significantly underestimated  $AV_S$  (Mainprice et al., 2008). Again, it is owing to the use of low cutoff energy and poorly converged results. The stereographic projection of the P-wave,  $V_P$ , shows that the propagation is slow perpendicular to the basal plane, i.e., along

the  $c$ -axis or [001] direction. The stereographic projection of  $AV_S$ , i.e., the difference between  $V_{S1}$  and  $V_{S2}$ , shows that  $AV_S$  is relatively large along the  $c$ -axis. The crystal symmetry has little or no effect on anisotropy (Fig. 6).

For an anisotropic mineral such as talc,  $V_P/V_S$  ratio can be further examined as  $V_P/V_{S1}$  and  $V_P/V_{S2}$  and their variations along pressures and propagation directions (Supplementary Data Fig. 9). It is noted that the different crystal symmetry has almost no effect on  $V_P/V_S$  ratio. Along the  $c$ -axis, i.e., [001] direction, the  $V_P/V_{S1}$  of both triclinic and monoclinic talc ranges between 1.4 and 1.5 over the entire explored pressure range and is relatively insensitive to compression. In contrast, the  $V_P/V_{S2}$  of talc is quite large and is  $\sim 5-7$  at zero pressure. Upon compression,  $V_P/V_{S2}$  of triclinic talc decreases to  $\sim 3.0$  at 1.5 GPa and  $\sim 2.1$  at 4 GPa, while  $V_P/V_{S2}$  of monoclinic



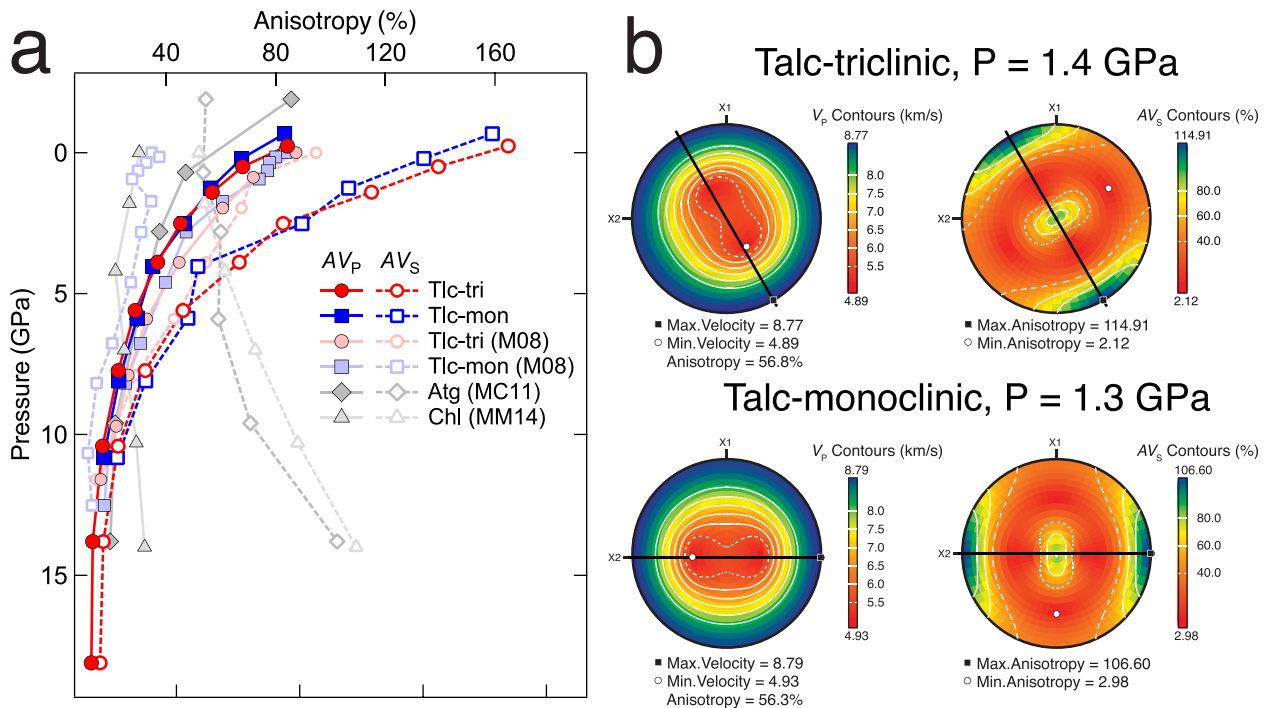


**Fig. 6.** (a) Compressional and shear wave anisotropy,  $AV_p$  and  $AV_s$ , as a function of pressure for various layered hydrous minerals relevant for the subduction zone settings. Mineral abbreviation: tlc-tri- talc-triclinic (this study; Mainprice et al., 2008); tlc-mon: talc-monoclinic (this study; Mainprice et al., 2008); atg- antigorite serpentine (Mookherjee and Capitani, 2011); and chl- chlorite (Mookherjee and Mainprice, 2014). (b) Stereographic projections down the c-axis of  $V_p$  and  $AV_s$  of both triclinic and monoclinic talc at  $\sim 1.3$ – $1.4$  GPa, which corresponds to a depth of  $\sim 45$  km. The black square symbols denote the maximum values, and the white circle symbols denote the minimum values. The solid black lines mark the fixed azimuth angle for Fig. 8c, i.e.,  $150^\circ$  for triclinic talc and  $90^\circ$  for monoclinic talc.

talc decreases to  $\sim 3.4$  at 1.5 GPa and  $\sim 2.1$  at 4 GPa. Beyond 4 GPa, the  $V_p/V_{S2}$  is largely insensitive to pressures. Moreover, for the randomly oriented talc aggregate, the bulk  $V_p/V_s$  of both triclinic and monoclinic talc ranges between 1.7 and 1.9 that is in-between the  $V_p/V_{S1}$  and  $V_p/V_{S2}$ . Additionally, the stereographic projection shows that the ratios vary a lot with propagation directions, especially  $V_p/V_{S2}$  (Supplementary Data Fig. 9).

#### 4.2. Poisson's ratio

When materials are compressed along a certain axis, they tend to expand in the direction perpendicular to the compression axis. The Poisson's ratio quantitatively captures this phenomenon. It is defined as the negative ratio of the transverse deformation to the axial deformation. It is expected that softer material will expand more with the unit compression force, resulting in a larger Poisson's ratio.

We estimated the Poisson's ratio of triclinic talc along various extension directions (Supplementary Method; Fig. 7). At low pressures, i.e., below 4 GPa, the Poisson's ratio is negative for many directions. This means that if talc is stretched along the axial direction, the transverse directions will also expand. This is a special class of materials known as "auxetic materials" (Yang et al., 2004). Talc exhibits auxetic behavior at low pressures, i.e.,  $P \leq \sim 4$  GPa. At  $\sim 1.4$  GPa, i.e., the depth of  $\sim 45$  km, the Poisson's ratio is as low as  $-0.62$ . It gradually transitions to a normal behavior at high pressures. For instance, at  $P \geq 5.6$  GPa, talc exhibits the normal positive Poisson's ratio in all directions (Fig. 7). We noted that Poisson's ratio is still very anisotropic at higher pressures. The Poisson's ratio varies greatly with different directions, and even in a certain direction, the maximum and minimum directions yield very different Poisson's ratios.

#### 5. Implication

In the central Mexican subduction zone, a series of seismological studies based on the Meso-America Subduction Experiment (MASE) have revealed the presence of an ultra-slow velocity layer between the subducting Cocos plate and the overriding North American plate (Fig. 8). This layer is characterized by a small thickness of  $\sim 2$ – $8$  km, low-velocity, low-viscosity, and low-strength (i.e., aseismic) (Pérez-Campos et al., 2008; Song et al., 2009; Kim et al., 2010, 2013; Manea and Manea, 2011; Dougherty et al., 2012). In addition to the existence of an ultra-slow velocity layer, the subduction zone is also unique because- (a) it has a shallow-flat-steep subduction configuration, and (b) the subducting slab is just located below the Moho and thus is almost devoid of overlying mantle wedge and directly overlain by the continental crust of North American plate. This thin, low-velocity, and weak layer is interpreted as being made up of either hydrated mineralogy (talc and chlorite) or high pore fluid pressures (Audet et al., 2009; Song and Kim, 2012).

Prior studies have also found that this flat segment of the slab is characterized by (a) a constant depth of  $\sim 45$  km; (b) a low shear velocity of  $2.4$ – $3.4$  km/s, i.e., even slower than the topmost of the slab by  $1.3$ – $1.5$  km/s; (c) a high  $V_p/V_s$  ratio of  $2.05 \pm 0.25$  based on a  $V_p$  of  $\sim 5.54$  km/s; and (d) a slab surface temperature of  $500$ – $800$  °C (Kim et al., 2010). Considering all these constraints, the pore fluid pressure is unlikely since the fluid is likely to be lost by this depth (Manea and Manea, 2011). In contrast, the hydrated mineral such as talc is likely to form by the reaction of serpentines and slab-derived silica-rich fluids along the slab-wedge interface which lies in the thermodynamic stability field of talc ( $\sim 800$  °C at  $1$ – $2$  GPa) (Bose and Ganguly, 1995; Pawley and Wood, 1995). In addition, geophysical observations on MASE did show that fluids

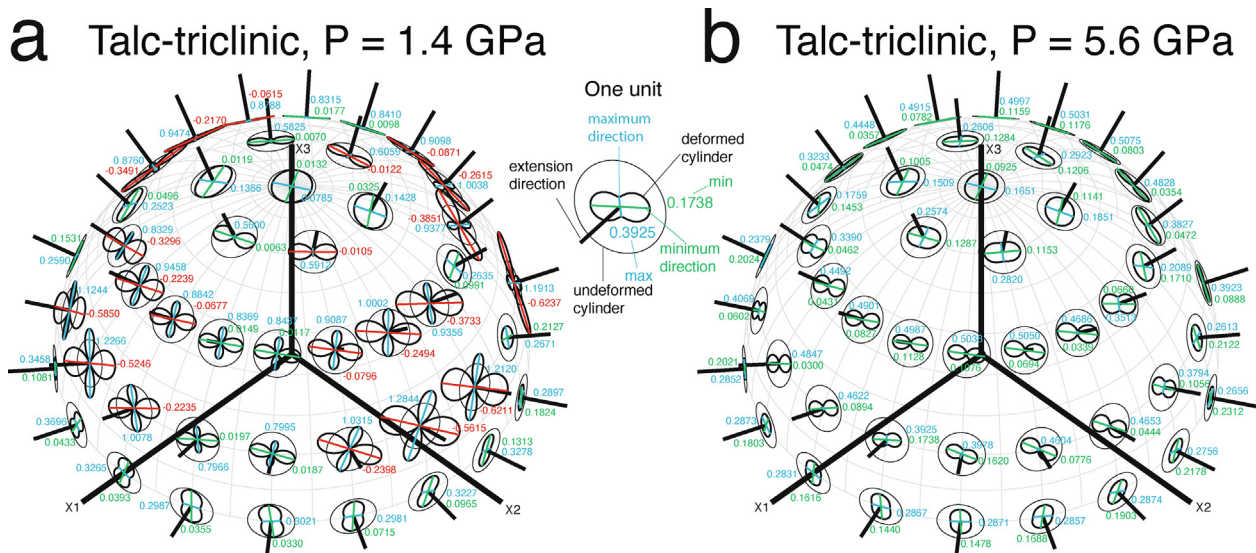


**Fig. 7.** Poisson's ratio of triclinic talc along different directions at (a) low and (b) high pressures, i.e., 1.4 and 5.6 GPa. In each unit on the three-dimensional upper hemisphere stereogram, the bold short black line at the center of the circle points to the extension direction; the thin circle represents the undeformed cylinder; the bold circle represents the elastically deformed cylinder with 1% elastic extension applied; the blue and green lines represent the maximum and minimum direction of Poisson's ratio, respectively; and the blue and green numbers are the maximum and minimum value of Poisson's ratio. It is noted that red lines and red numbers in panel (a) indicate that Poisson's ratio is negative.

release due to slab dehydration and then hydrate the upper plate. For example, a  $\sim 13$  km thick continental root is expected below the 2.2 km elevation of the Trans-Mexican Volcanic Belt based on isostatic equilibrium, but it is missing. Instead, low-density minerals induced by hydration are suggested to compensate for the negative buoyancy (Kim et al., 2010). Also, several regions of non-volcanic tremor have been reported above the flat slab suggesting lasting hydration and weakening of the overlying continental crust (Fig. 8) (Manea and Manea, 2011). Thus talc is a potential candidate for explaining the ultra-slow velocity layer in central Mexico (Kim et al., 2013).

However, apart from being thermodynamically stable, talc also needs to fulfill the crucial constraints of low shear velocity and high  $V_p/V_s$  ratio observed in this subduction zone setting. We evaluated the potentiality of talc to explain the ultra-slow velocity layer using our predicted elasticity and anisotropy. We compiled the reported  $V_p/V_s$  vs.  $V_s$  in the central Mexican subduction zone (Kim et al., 2010). We compared the geophysical compilation with that of relevant hydrous minerals, including lizardite, antigorite, phlogopite, and chlorite (Mookherjee and Stixrude, 2009; Bezacier et al., 2010; Chheda et al., 2014; Mantihalake et al., 2021) (Fig. 8). At  $\sim 1.5$  GPa, i.e.,  $\sim 45$  km depth, the  $V_p/V_{S1}$  ratio of triclinic talc varies between 1.2 and 1.8 and  $V_p/V_{S2}$  varies between 1.2 and 6.3 with the bulk  $V_p/V_s \sim 1.7$ . At similar conditions, the  $V_p/V_{S1}$  of monoclinic talc varies between 1.1 and 1.8 and  $V_p/V_{S2}$  varies between 1.2 and 5.6 with the bulk  $V_p/V_s \sim 1.8$  (Supplementary Data Fig. 9). The bulk  $V_p/V_s$  assumes an inherently homogenous nature, i.e., random orientation, of the minerals/rocks, while the  $V_p/V_{S1}$  and  $V_p/V_{S2}$  are estimated along specific propagation directions. However, it is likely for talc to develop a strong crystallographic preferred orientation along interfaces between subduction slab and mantle wedge (Lee et al., 2020; Nagaya et al., 2020). The range of  $V_p/V_s$  for talc due to different propagation directions can explain the  $V_p/V_s$  ratio as high as  $2.05 \pm 0.25$  observed in the ultra-slow velocity layer of the central Mexican subduction zone.

Seismologically, the strength and geometry of anisotropy are generally reflected by the delay time between the fast and slow shear waves and the polarization direction of the fast shear wave, respectively (Long and van der Hilst, 2006; Faccenda et al., 2008;

Long and Silver, 2008). Many subduction zones, including Ryukyu and Tonga, are often characterized by a large delay time of  $> 1$  s (Long and Silver, 2008; Katayama et al., 2009). The delay time is proportional to the ray path length and the strength of anisotropy along the ray path. Although olivine is the dominant mantle mineral, the elastic anisotropy of olivine is  $\sim 10\%$ , and significant thickness of mantle with preferred orientated olivine is required to explain a large delay time. In contrast, the extremely anisotropic mineral such as talc could easily explain the large delay time within a thin layer. To further illustrate the degree of anisotropy associated with talc, we took the central Mexican subduction zone as an example. If we were to assume a talc layer of  $\sim 4 \pm 1$  km thick (Song et al., 2009; Kim et al., 2010, 2013; Manea and Manea, 2011), the estimated delay time is likely to be  $\sim 0.03 \pm 0.01$  s to  $2.1 \pm 0.5$  s depending on the incidence angle based on the single-crystal anisotropy of triclinic talc. The largest delay time is observed when the ray path is parallel to the (001) plane of talc, i.e., along  $a$ - $b$  plane of triclinic talc with the azimuth angle of  $150^\circ$  (Fig. 6). Similarly, the predicted delay time for monoclinic talc is  $\sim 0.04 \pm 0.01$  s to  $1.8 \pm 0.4$  s. The largest delay time is observed when the ray path is parallel to the (001) plane and along the  $b$ -axis of monoclinic talc (Fig. 6). However, since talc is extremely anisotropic, the predicted delay time along the  $c$ -axis is still very high, with triclinic and monoclinic talc being  $\sim 1.8 \pm 0.4$  s and  $1.5 \pm 0.4$  s, respectively. Clearly, a relatively thin layer of extremely anisotropic minerals such as talc could easily explain the large delay time  $> 1$  s, assuming a perfect crystal alignment. However, our understanding of the elasticity of talc in subduction zone settings is likely to be enhanced by further investigations on the slip system and how non-hydrostatic stresses are likely to affect the crystallographic preferred orientation of talc-bearing lithology.

## 6. Conclusions

We explored the structure, equation of state, and elasticity of both triclinic and monoclinic talc under high pressures up to 18 GPa using *first principles* simulations based on density functional theory corrected for dispersive forces. Owing to the dispersive correction and high cutoff energy of 900 eV, our results are

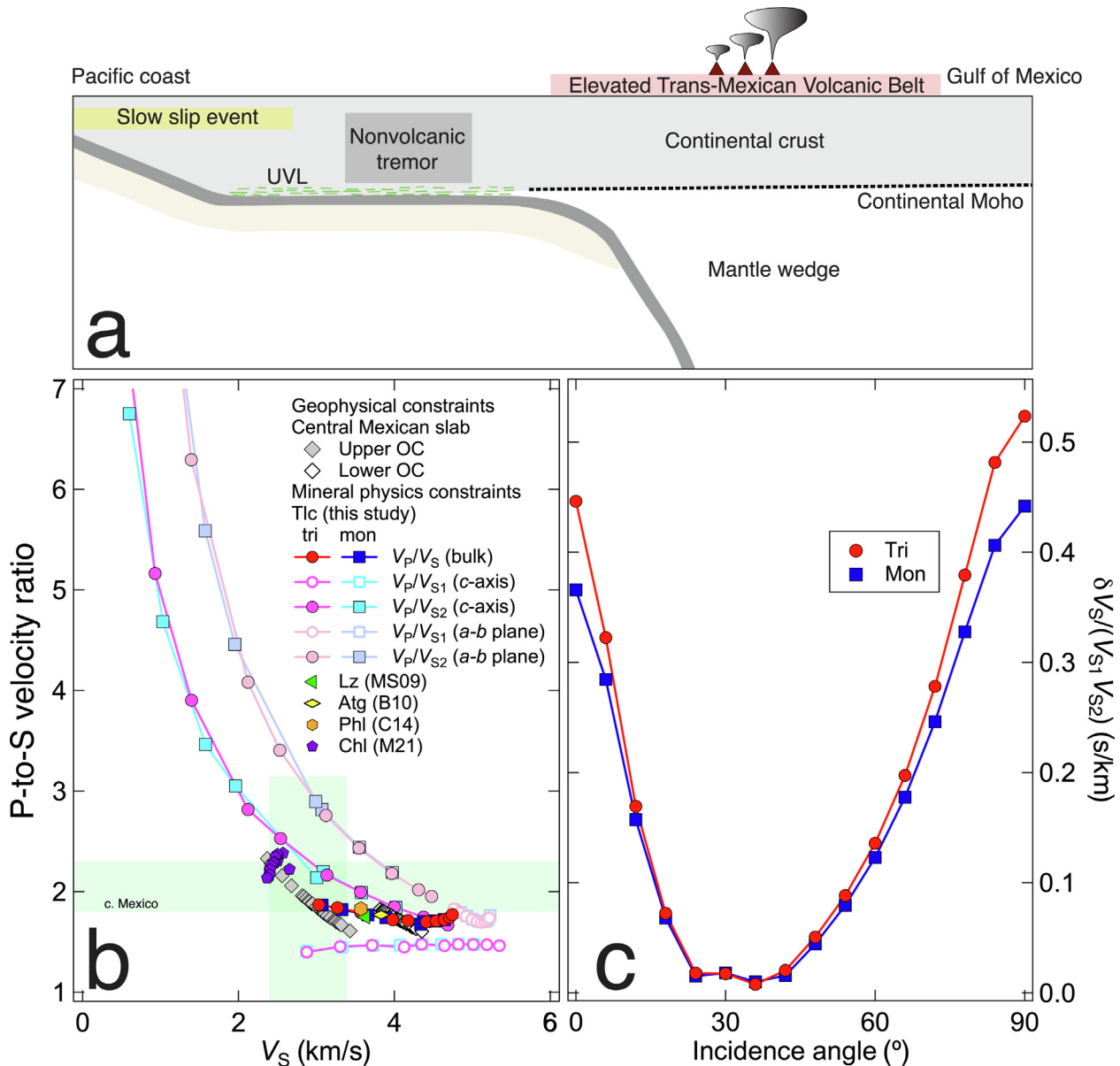


**Fig. 8.** (a) Schematic diagram of the central Mexican subduction zone with the shallow-flat-steep subduction configuration. In the ultra-slow velocity layer (UVL), it is assumed that the (001) plane of talc is nearly parallel to the flat slab, marked by the green bars. (b) P-to-S velocity ratio ( $V_P/V_S$ ) vs. shear wave velocity  $V_S$  of talc. Our results are compared with various layered hydrous minerals relevant for the subduction zone settings, including lizardite serpentine (lz) (Mookherjee and Stixrude, 2009), antigorite serpentine (atg) (Bezacier et al., 2010), phlogopite (phl) (Chheda et al., 2014), and chlorite (chl) (Manthilake et al., 2021). The gray and open diamonds represent the data of the upper and lower oceanic crustal (OC) layer of the subducting slab of the central Mexican subduction zone (Kim et al., 2010). (c) Delay time/ thickness of the anisotropic layer ( $\delta V_S / (V_{S1} V_{S2})$ ) as a function of incidence angle of both triclinic and monoclinic talc at  $\sim 1.3\text{--}1.4$  GPa, which corresponds to a depth of  $\sim 45$  km. The profile of the data is marked by the solid black lines in Fig. 6, i.e., the azimuth angle is  $150^\circ$  for triclinic talc and  $90^\circ$  for monoclinic talc. The incidence angle is between the ray path and c-axis, i.e.,  $0^\circ$  indicates the ray path is along the c-axis while  $90^\circ$  indicates the ray path is parallel to a-b plane.

significantly improved compared to the previous high-pressure elasticity study (Mainprice et al., 2008). The prior estimations were widely used to explain the geophysical observations or build geophysical models relevant to subduction zone settings. However, our results indicate that the prior studies greatly overestimated the shear moduli and shear wave velocity and significantly underestimated the shear wave anisotropy. Thus, the new set of elasticity and anisotropy data warrants re-evaluation of the velocity models and/or subsequent geophysical interpretations.

Our results also show that some components of the full elastic constant tensor, including  $C_{11}$ ,  $C_{22}$ , and  $C_{66}$ , exhibit anomalous pressure dependence. The non-monotonic pressure dependence of elastic constant components is very likely related to the struc-

tural changes, which usually manifests in a polytypic transition from a low-pressure polytype talc-I to a high-pressure polytype talc-II. This polytypic transition occurs at  $\sim 3$  GPa, which is within the thermodynamic stability field of talc. The transition could be a structural precursor of the 10-Å phase, a hydrous mineral that is thermodynamically stable at a deeper depth and is crucial for transporting water into the deep Earth.

Our study also shows that talc bearing hydrated lithology could readily account for anomalously low velocity, extremely high anisotropy, and anomalously high  $V_P/V_S$  ratio observed in subduction zone settings. In addition, talc bearing lithologies could also explain a large delay time in shear wave splitting as observed from seismological studies in many subduction systems.

## Declaration of Competing Interest

The authors declare that they have no known competing financial interests or personal relationships that could have appeared to influence the work reported in this paper.

## Acknowledgments

This work is supported by the US National Science Foundation grant EAR 1763215 and EAR 1753125. YP and MM acknowledge computing resources from XSEDE facilities (GEO170003) and the High-Performance Computing, Research Computing Center, Florida State University. AH acknowledges computing resources from the UK's National Supercomputer Service through the UK Car-parrinello Consortium (EPSRC Grant No. EP/P022561/1) and project ID d56 "Planetary Interiors". GM acknowledges funding from the INSU-CNRS and the French Government Laboratory of Excellence initiative n°ANR-10-LABX-0006, the Région Auvergne, and the European Regional Development Fund (ClerVolc contribution number 530).

## Appendix A. Supplementary data

Supplementary data to this article can be found online at <https://doi.org/10.1016/j.gsf.2022.101381>.

## References

- Angel, R.J., 2000. Equations of state. *Rev. Mineral. Geochem.* 41, 35–59. <https://doi.org/10.2138/rmg.2000.41.2>.
- Audet, P., Bostock, M.G., Christensen, N.I., Peacock, S.M., 2009. Seismic evidence for overpressured subducted oceanic crust and megathrust fault sealing. *Nature* 457, 76–78. <https://doi.org/10.1038/nature07650>.
- Auzende, A.L., Daniel, I., Reynard, B., Lemaire, C., Guyot, F., 2004. High-pressure behaviour of serpentine minerals: a Raman spectroscopic study. *Phys. Chem. Miner.* 31, 269–277. <https://doi.org/10.1007/s00269-004-0384-0>.
- Basu, A., Mookherjee, M., 2021. Intercalation of water in kaolinite (Al<sub>2</sub>Si<sub>2</sub>O<sub>5</sub>(OH)<sub>4</sub>) at subduction zone conditions: insights from Raman Spectroscopy. *ACS Earth Space Chem.* 5, 834–848. <https://doi.org/10.1021/acsearthspacechem.0c00349>.
- Babeyko, A.Y., Sobolev, S.V., Sinelnikov, E.D., Smirnov, Y.P., Deresvichkova, N.A., 1994. Calculation of elastic properties in lower part of the Kola borehole from bulk chemical compositions of core samples. *Surv. Geophys.* 15, 545–573. <https://doi.org/10.1007/BF00690174>.
- Bailey, E., Holloway, J.R., 2000. Experimental determination of elastic properties of talc to 800 °C, 0.5 GPa; calculations of the effect on hydrated peridotite, and implications for cold subduction zones. *Earth Planet. Sci. Lett.* 183, 487–498. [https://doi.org/10.1016/S0012-821X\(00\)00288-0](https://doi.org/10.1016/S0012-821X(00)00288-0).
- Bebout, G.E., Barton, M.D., 2002. Tectonic and metasomatic mixing in a high-T, subduction-zone mélange—insights into the geochemical evolution of the slab-mantle interface. *Chem. Geol.* 187, 79–106. [https://doi.org/10.1016/S0009-2541\(02\)00019-0](https://doi.org/10.1016/S0009-2541(02)00019-0).
- Bezacier, L., Reynard, B., Bass, J.D., Sanchez-Valle, C., Van de Moortèle, B., 2010. Elasticity of antigorite, seismic detection of serpentinites, and anisotropy in subduction zones. *Earth Planet. Sci. Lett.* 289, 198–208. <https://doi.org/10.1016/j.epsl.2009.11.009>.
- Bezacier, L., Reynard, B., Cardon, H., Montagnac, G., Bass, J.D., 2013. High-pressure elasticity of serpentine and seismic properties of the hydrated mantle wedge. *J. Geophys. Res.: Solid Earth* 118, 527–535. <https://doi.org/10.1002/jgrb.50076>.
- Birch, F., 1978. Finite strain isotherm and velocities for single-crystal and polycrystalline NaCl at high pressures and 300 K. *J. Geophys. Res.: Solid Earth* 83, 1257–1268. <https://doi.org/10.1029/JB083iB03p01257>.
- Boschi, C., Früh-Green, G.L., Escartín, J., 2006. Occurrence and significance of serpentinite-hosted, talc-and amphibole-rich fault rocks in modern oceanic settings and ophiolite complexes: An overview. *Ophioliti* 31, 129–140. <https://doi.org/10.4454/ofioliti.v31i2.335>.
- Bose, K., Ganguly, J., 1995. Experimental and theoretical studies of the stabilities of talc, antigorite and phase A at high pressures with applications to subduction processes. *Earth Planet. Sci. Lett.* 136, 109–121. [https://doi.org/10.1016/0012-821X\(95\)00188-1](https://doi.org/10.1016/0012-821X(95)00188-1).
- Brudzinski, M.R., Thurber, C.H., Hacker, B.R., Engdahl, E.R., 2007. Global prevalence of double Benioff zones. *Science* 316, 1472–1474. <https://doi.org/10.1126/science.1139204>.
- Chantel, J., Mookherjee, M., Frost, D.J., 2012. The elasticity of lawsonite at high pressure and the origin of low velocity layers in subduction zones. *Earth Planet. Sci. Lett.* 349, 116–125. <https://doi.org/10.1016/j.epsl.2012.06.034>.
- Chhedra, T.D., Mookherjee, M., Mainprice, D., dos Santos, A.M., Molaison, J.J., Chantel, J., Manthilake, G., Bassett, W.A., 2014. Structure and elasticity of phlogopite under compression: geophysical implications. *Phys. Earth Planet. Inter.* 233, 1–12. <https://doi.org/10.1016/j.pepi.2014.05.004>.
- Davies, G.F., 1974. Effective elastic moduli under hydrostatic stress—I. quasi-harmonic theory. *J. Phys. Chem. Solids* 35, 1513–1520. [https://doi.org/10.1016/S0022-3697\(74\)80279-9](https://doi.org/10.1016/S0022-3697(74)80279-9).
- Dera, P., Prewitt, C.T., Japel, S., Bish, D.L., Johnston, C.T., 2003. Pressure-controlled polytypism in hydrous layered materials. *Am. Mineral.* 88, 1428–1435. <https://doi.org/10.2138/am-2003-1006>.
- Dion, M., Rydberg, H., Schröder, E., Langreth, D.C., Lundqvist, B.I., 2004. Van der Waals density functional for general geometries. *Phys. Rev. Lett.* 92, 246401. <https://doi.org/10.1103/PhysRevLett.92.246401>.
- Dorbath, C., Gerbault, M., Carlier, G., Guiraud, M., 2008. Double seismic zone of the Nazca plate in northern Chile: high-resolution velocity structure, petrological implications, and thermomechanical modeling. *Geochem. Geophys. Geosyst.* 9, Q07006. <https://doi.org/10.1029/2008GC002020>.
- Dougherty, S.L., Clayton, R.W., Helmberger, D.V., 2012. Seismic structure in central Mexico: Implications for fragmentation of the subducted Cocos plate. *J. Geophys. Res.: Solid Earth* 117, B09316. <https://doi.org/10.1029/2012JB009528>.
- Escartín, J., Andreani, M., Hirth, G., Evans, B., 2008. Relationships between the microstructural evolution and the rheology of talc at elevated pressures and temperatures. *Earth Planet. Sci. Lett.* 268, 463–475. <https://doi.org/10.1016/j.epsl.2008.02.004>.
- Evans, B.W., Johannes, W., Oterdoom, W.H., Trommsdorff, V., 1976. Stability of chrysotile and antigorite in the serpentine multisystem. *Schweiz. Mineral. Petrogr. Mitt.* 56, 79–93.
- Faccenda, M., Burlini, L., Gerya, T.V., Mainprice, D., 2008. Fault-induced seismic anisotropy by hydration in subducting oceanic plates. *Nature* 455, 1097–1100. <https://doi.org/10.1038/nature07376>.
- Gatta, G.D., Merlini, M., Valdrè, G., Liermann, H.P., Nénert, G., Rothkirch, A., Kahlenberg, V., Pavese, A., 2013. On the crystal structure and compressional behavior of talc: a mineral of interest in petrology and material science. *Phys. Chem. Miner.* 40, 145–156. <https://doi.org/10.1007/s00269-012-0554-4>.
- Gleason, A.E., Parry, S.A., Pawley, A.R., Jeanloz, R., Clark, S.M., 2008. Pressure-temperature studies of talc plus water using X-ray diffraction. *Am. Mineral.* 93, 1043–1050. <https://doi.org/10.2138/am.2008.2742>.
- Gruner, J.W., 1934. The crystal structures of talc and pyrophyllite. *Z. Kristallogr. – Cryst. Mater.* 88, 412–419. <https://doi.org/10.1524/zkri.1934.88.1.412>.
- Hirschmann, M.M., 2006. Water, melting, and the deep Earth H<sub>2</sub>O cycle. *Annu. Rev. Earth Planet. Sci.* 34, 629–653. <https://doi.org/10.1146/annurev.earth.34.031405.125211>.
- Hohenberg, P., Kohn, W., 1964. Inhomogeneous electron gas. *Phys. Rev.* 136, B864. <https://doi.org/10.1103/PhysRev.136.B864>.
- Johnston, C.T., Wang, S.L., Bish, D.L., Dera, P., Agnew, S.F., Kenney III, J.W., 2002. Novel pressure-induced phase transformations in hydrous layered materials. *Geophys. Res. Lett.* 29, 17-1-17-4. <http://dx.doi.org/10.1029/2002GL015402>.
- Karato, S.I., 2008. *Deformation of Earth Materials: An Introduction to the Rheology of Solid Earth*. Cambridge University Press, Cambridge, UK.
- Katayama, I., Hirauchi, K.I., Michibayashi, K., Ando, J.I., 2009. Trench-parallel anisotropy produced by serpentine deformation in the hydrated mantle wedge. *Nature* 461, 1114–1117. <https://doi.org/10.1038/nature08513>.
- Katsura, T., Tange, Y., 2019. A simple derivation of the Birch-Murnaghan Equations of State (EOSs) and comparison with EOSs derived from other definitions of finite strain. *Minerals* 9, 745. <https://doi.org/10.3390/min9120745>.
- Kawasaki, I., 2004. Silent earthquakes occurring in a stable-unstable transition zone and implications for earthquake prediction. *Earth Planets Space* 56, 813–821. <https://doi.org/10.1186/BF03353088>.
- Kim, Y., Clayton, R.W., Jackson, J.M., 2010. Geometry and seismic properties of the subducting Cocos plate in central Mexico. *J. Geophys. Res.: Solid Earth* 115, B06310. <https://doi.org/10.1029/2009JB006942>.
- Kim, Y., Clayton, R.W., Asimow, P.D., Jackson, J.M., 2013. Generation of talc in the mantle wedge and its role in subduction dynamics in central Mexico. *Earth Planet. Sci. Lett.* 384, 81–87. <https://doi.org/10.1016/j.epsl.2013.10.006>.
- Klimeš, J., Bowler, D.R., Michaelides, A., 2009. Chemical accuracy for the van der Waals density functional. *J. Phys.: Condens. Matter* 22, 022201. <https://doi.org/10.1088/0953-8984/22/2/022201>.
- Klimeš, J., Bowler, D.R., Michaelides, A., 2011. Van der Waals density functionals applied to solids. *Phys. Rev. B* 83, 195131. <https://doi.org/10.1103/PhysRevB.83.195131>.
- Kohn, W., Sham, L.J., 1965. Self-consistent equations including exchange and correlation effects. *Phys. Rev.* 140, A1133. <https://doi.org/10.1103/PhysRev.140.A1133>.
- Kresse, G., Furthmüller, J., 1996a. Efficiency of ab-initio total energy calculations for metals and semiconductors using a plane-wave basis set. *Comput. Mater. Sci.* 6, 15–50. [https://doi.org/10.1016/0927-0256\(96\)00008-0](https://doi.org/10.1016/0927-0256(96)00008-0).
- Kresse, G., Furthmüller, J., 1996b. Efficient iterative schemes for *ab initio* total-energy calculations using a plane-wave basis set. *Phys. Rev. B* 54, 11169. <https://doi.org/10.1103/PhysRevB.54.11169>.
- Kresse, G., Hafner, J., 1993. *Ab initio* molecular dynamics for liquid metals. *Phys. Rev. B* 47, 558. <https://doi.org/10.1103/PhysRevB.47.558>.
- Kresse, G., Joubert, D., 1999. From ultrasoft pseudopotentials to the projector augmented-wave method. *Phys. Rev. B* 59, 1758. <https://doi.org/10.1103/PhysRevB.59.1758>.
- Lee, J., Jung, H., Klemm, R., Tarling, M.S., Konopelko, D., 2020. Lattice preferred orientation of talc and implications for seismic anisotropy in subduction zones. *Earth Planet. Sci. Lett.* 537, <https://doi.org/10.1016/j.epsl.2020.116178>.

- Lee, J., Mookherjee, M., Kim, T., Jung, H., Klemd, R., 2021. Seismic anisotropy in subduction zones: evaluating the role of chloritoid. *Front. Earth Sci.* 9 644958. <https://doi.org/10.3389/feart.2021.644958>.
- Long, M.D., Silver, P.G., 2008. The subduction zone flow field from seismic anisotropy: A global view. *Science* 319, 315–318. <https://doi.org/10.1126/science.1150809>.
- Long, M.D., van der Hilst, R.D., 2006. Shear wave splitting from local events beneath the Ryukyu arc: Trench-parallel anisotropy in the mantle wedge. *Phys. Earth Planet. Inter.* 155, 300–312. <https://doi.org/10.1016/j.pepi.2006.01.003>.
- Mainprice, D., 1990. A FORTRAN program to calculate seismic anisotropy from the lattice preferred orientation of minerals. *Comput. Geosci.* 16, 385–393. [https://doi.org/10.1016/0098-3004\(90\)90072-2](https://doi.org/10.1016/0098-3004(90)90072-2).
- Mainprice, D., Le Page, Y., Rodgers, J., Jouanna, P., 2008. *Ab initio* elastic properties of talc from 0 to 12 GPa: Interpretation of seismic velocities at mantle pressures and prediction of auctetic behaviour at low pressure. *Earth Planet. Sci. Lett.* 274, 327–338. <https://doi.org/10.1016/j.epsl.2008.07.047>.
- Manea, V., Gurnis, M., 2007. Subduction zone evolution and low viscosity wedges and channels. *Earth Planet. Sci. Lett.* 264, 22–45. <https://doi.org/10.1016/j.epsl.2007.08.030>.
- Manea, V., Manea, M., 2011. Flat-slab thermal structure and evolution beneath central Mexico. *Pure Appl. Geophys.* 168, 1475–1487. <https://doi.org/10.1007/s00024-010-0207-9>.
- Manthilake, G., Chantel, J., Guignot, N., King, A., 2021. The anomalous seismic behavior of aqueous fluids released during dehydration of chlorite in subduction zones. *Minerals* 11, 70. <https://doi.org/10.3390/min11010070>.
- Marschall, H.R., Schumacher, J.C., 2012. Arc magmas sourced from mélange diapirs in subduction zones. *Nat. Geosci.* 5, 862–867. <https://doi.org/10.1038/ngeo1634>.
- Meade, C., Jeanloz, R., 1990. Static compression of  $\text{Ca}(\text{OH})_2$  at room temperature: observations of amorphization and equation of state measurements to 10.7 GPa. *Geophys. Res. Lett.* 17, 1157–1160. <https://doi.org/10.1029/GL017i008p01157>.
- Monkhorst, H.J., Pack, J.D., 1976. Special points for Brillouin-zone integrations. *Phys. Rev. B* 13, 5188. <https://doi.org/10.1103/PhysRevB.13.5188>.
- Mookherjee, M., Capitani, G.C., 2011. Trench parallel anisotropy and large delay times: Elasticity and anisotropy of antigorite at high pressures. *Geophys. Res. Lett.* 38, L09315. <https://doi.org/10.1029/2011GL047160>.
- Mookherjee, M., Mainprice, D., 2014. Unusually large shear wave anisotropy for chlorite in subduction zone settings. *Geophys. Res. Lett.* 41, 1506–1513. <https://doi.org/10.1002/2014GL059334>.
- Mookherjee, M., Stixrude, L., 2009. Structure and elasticity of serpentine at high-pressure. *Earth Planet. Sci. Lett.* 279, 11–19. <https://doi.org/10.1016/j.epsl.2008.12.018>.
- Mookherjee, M., Tsuchiya, J., Hariharan, A., 2016. Crystal structure, equation of state, and elasticity of hydrous aluminosilicate phase, topaz-OH ( $\text{Al}_2\text{Si}_2\text{O}_7(\text{OH})_2$ ) at high pressures. *Phys. Earth Planet. Inter.* 251, 24–35. <https://doi.org/10.1016/j.pepi.2015.11.006>.
- Mookherjee, M., Panero, W.R., Wunder, B., Jahn, S., 2019. Anomalous elastic behavior of phase Egg,  $\text{AlSiO}_3(\text{OH})$ , at high pressures. *Am. Mineral.* 104, 130–139. <https://doi.org/10.2138/am-2019-6694>.
- Mookherjee, M., Speziale, S., Marquardt, H., Jahn, S., Wunder, B., Koch-müller, M., Liermann, H.-P., 2015. Equation of state and elasticity of 3.65 Å phase-implications for the X-discontinuity. *Am. Mineral.* 100, 2199–2208. <https://doi.org/10.2138/am-2015-5312>.
- Mookherjee, M., Tsuchiya, J., 2015. Elasticity of superhydrous phase, B,  $\text{Mg}_{10}\text{Si}_4\text{O}_{14}(\text{OH})_4$ . *Phys. Earth Planet. Inter.* 238, 42–50. <https://doi.org/10.1016/j.pepi.2014.10.010>.
- Moore, D.E., Lockner, D.A., 2008. Talc friction in the temperature range 25–400 °C: Relevance for fault-zone weakening. *Tectonophysics* 449, 120–132. <https://doi.org/10.1016/j.tecto.2007.11.039>.
- Moore, D.E., Rymer, M.J., 2007. Talc-bearing serpentinite and the creeping section of the San Andreas fault. *Nature* 448, 795–797. <https://doi.org/10.1038/nature06064>.
- Murnaghan, F.D., 1937. A theory of elasticity. *Phys. Rev.* 51, 593. <https://doi.org/10.1103/PhysRev.51.593>.
- Nagaya, T., Okamoto, A., Oyanagi, R., Seto, Y., Miyake, A., Uno, M., Muto, J., Wallis, S. R., 2020. Crystallographic preferred orientation of talc determined by an improved EBSD procedure for sheet silicates: Implications for anisotropy at the slab-mantle interface due to Si-metasomatism. *Am. Mineral.* 105, 873–893. <https://doi.org/10.2138/am-2020-7006>.
- Nestola, F., Angel, R.J., Zhao, J., Garrido, C.J., Sanchez-Vizcano, V.L., Capitani, G., Mellini, M., 2010. Antigorite equation of state and anomalous softening at 6 GPa: an in situ single-crystal X-ray diffraction study. *Contrib. Mineral. Petrol.* 160, 33–43. <https://doi.org/10.1007/s00410-009-0463-9>.
- Nye, J.F., 1985. *Physical Properties of Crystals: Their Representation by Tensors and Matrices*. Oxford University Press, Oxford, UK.
- Ohtani, E., Litasov, K., Hosoya, T., Kubo, T., Kondo, T., 2004. Water transport into the deep mantle and formation of a hydrous transition zone. *Phys. Earth Planet. Inter.* 143, 255–269. <https://doi.org/10.1016/j.pepi.2003.09.015>.
- Pawley, A.R., Wood, B.J., 1995. The high-pressure stability of talc and 10 Å phase: potential storage sites for  $\text{H}_2\text{O}$  in subduction zones. *Am. Mineral.* 80, 998–1003. <https://doi.org/10.2138/am-1995-9-1015>.
- Pawley, A.R., Clark, S.M., Chinnery, N.J., 2002. Equation of state measurements of chlorite, pyrophyllite, and talc. *Am. Mineral.* 87, 1172–1182. <https://doi.org/10.2138/am-2002-8-916>.
- Pawley, A.R., Redfern, S.A., Wood, B.J., 1995. Thermal expansivities and compressibilities of hydrous phases in the system  $\text{MgO-SiO}_2\text{-H}_2\text{O}$ : talc, phase A and 10-Å phase. *Contrib. Mineral. Petrol.* 122, 301–307. <https://doi.org/10.1007/s004100050129>.
- Peacock, S.M., Hyndman, R.D., 1999. Hydrous minerals in the mantle wedge and the maximum depth of subduction thrust earthquakes. *Geophys. Res. Lett.* 26, 2517–2520. <https://doi.org/10.1029/1999GL900558>.
- Peng, Y., Mookherjee, M., 2020. Thermoelasticity of tremolite amphibole: Geophysical implications. *Am. Mineral.* 105, 904–916. <https://doi.org/10.2138/am-2020-7189>.
- Peng, Y., Mookherjee, M., Hermann, A., Bajgain, S., Liu, S., Wunder, B., 2017. Elasticity of phase-Pi ( $\text{Al}_3\text{Si}_2\text{O}_7(\text{OH})_3$ )—A hydrous aluminosilicate phase. *Phys. Earth Planet. Inter.* 269, 91–97. <https://doi.org/10.1016/j.pepi.2017.05.016>.
- Perdew, J.P., Burke, K., Ernzerhof, M., 1996. Generalized gradient approximation made simple. *Phys. Rev. Lett.* 77, 3865. <https://doi.org/10.1103/PhysRevLett.77.3865>.
- Perdikatsis, B., Burlzaff, H., 1981. Strukturverfeinerung am talk  $\text{Mg}_3[(\text{OH})_2\text{Si}_4\text{O}_{10}]$ . *Z. Kristallogr. - Cryst. Mater.* 156, 177–186. <https://doi.org/10.1524/zkri.1981.156.3-4.177>.
- Pérez-Campos, X., Kim, Y., Husker, A., Davis, P.M., Clayton, R.W., Iglesias, A., Pacheco, J.F., Singh, S.K., Manea, V., Gurnis, M., 2008. Horizontal subduction and truncation of the Cocos Plate beneath central Mexico. *Geophys. Res. Lett.* 35, L18303. <https://doi.org/10.1029/2008GL035127>.
- Ranero, C.R., Morgan, J.P., McIntosh, K., Reichert, C., 2003. Bending-related faulting and mantle serpentinization at the Middle America trench. *Nature* 425, 367–373. <https://doi.org/10.1038/nature01961>.
- Rashchenko, S.V., Likhacheva, A.Y., Goryainov, S.V., Krylov, A.S., Litasov, K.D., 2016. In situ spectroscopic study of water intercalation into talc: New features of 10 Å phase formation. *Am. Mineral.* 101, 431–436. <https://doi.org/10.2138/am-2016-5356>.
- Rayner, J.H., Brown, G., 1973. The crystal structure of talc. *Clays Clay Miner.* 21, 103–114. <https://doi.org/10.1346/CCMN.1973.0210206>.
- Román-Pérez, G., Soler, J.M., 2009. Efficient implementation of a van der Waals density functional: application to double-wall carbon nanotubes. *Phys. Rev. Lett.* 103. <https://doi.org/10.1103/PhysRevLett.103.096102>.
- Rondenay, S., Abers, G.A., Van Keken, P.E., 2008. Seismic imaging of subduction zone metamorphism. *Geology* 36, 275–278. <https://doi.org/10.1130/G24112A.1>.
- Schroeder, T., John, B.E., 2004. Strain localization on an oceanic detachment fault system, Atlantis Massif, 30 N, Mid-Atlantic Ridge. *Geochem. Geophys. Geosyst.* 5, Q11007. <https://doi.org/10.1029/2004GC000728>.
- Saha, S., Peng, Y., Dasgupta, R., Mookherjee, M., Fischer, K.M., 2021. Assessing the presence of volatile-bearing mineral phases in cratonic mantle as a possible cause of mid-lithospheric discontinuities. *Earth Planet. Sci. Lett.* 553. <https://doi.org/10.1016/j.epsl.2020.116602>.
- Scott, H.P., Liu, Z., Hemley, R.J., Williams, Q., 2007. High-pressure infrared spectra of talc and lawsonite. *Am. Mineral.* 92, 1814–1820. <https://doi.org/10.2138/am.2007.2430>.
- Song, T., Kim, Y., 2012. Anisotropic uppermost mantle in young subducted slab underplating Central Mexico. *Nat. Geosci.* 5, 55–59. <https://doi.org/10.1038/ngeo1342>.
- Song, T., Helmberger, D.V., Brudzinski, M.R., Clayton, R.W., Davis, P., Pérez-Campos, X., Singh, S.K., 2009. Subducting slab ultra-slow velocity layer coincident with silent earthquakes in southern Mexico. *Science* 324, 502–506. <https://doi.org/10.1126/science.1167595>.
- Spandler, C., Hermann, J., Faure, K., Mavrogenes, J.A., Arculus, R.J., 2008. The importance of talc and chlorite “hybrid” rocks for volatile recycling through subduction zones; evidence from the high-pressure subduction mélange of New Caledonia. *Contrib. Mineral. Petrol.* 155, 181–198. <https://doi.org/10.1007/s00410-007-0236-2>.
- Stixrude, L., 2002. Talc under tension and compression: Spinodal instability, elasticity, and structure. *J. Geophys. Res.: Solid Earth* 107, 2327. <https://doi.org/10.1029/2001JB001684>.
- Tsuchiya, J., 2013. A first-principles calculation of the elastic and vibrational anomalies of lizardite under pressure. *Am. Mineral.* 98, 2046–2052. <https://doi.org/10.2138/am.2013.4369>.
- Tsuchiya, J., Tsuchiya, T., 2009. Elastic properties of  $\delta$ -AlOOH under pressure: First principles investigation. *Phys. Earth Planet. Inter.* 174, 122–127. <https://doi.org/10.1016/j.pepi.2009.01.008>.
- Tsuchiya, J., Tsuchiya, T., 2011. First-principles prediction of a high-pressure hydrous phase of AlOOH. *Phys. Rev. B* 83. <https://doi.org/10.1103/PhysRevB.83.054115>.
- Tsuchiya, J., Tsuchiya, T., Tsuneyuki, S., 2005. First-principles study of hydrogen bond symmetrization of phase D under high pressure. *Am. Mineral.* 90, 44–49. <https://doi.org/10.2138/am.2005.1628>.
- Ulian, G., Valdrè, G., 2017. Effects of fluorine content on the elastic behavior of topaz  $[\text{Al}_2\text{SiO}_4(\text{F}, \text{OH})_2]$ . *Am. Mineral.* 102, 347–356. <https://doi.org/10.2138/am-2017-5668>.
- Ulian, G., Valdrè, G., 2019. Equation of state and second-order elastic constants of portlandite  $\text{Ca}(\text{OH})_2$  and brucite  $\text{Mg}(\text{OH})_2$ . *Phys. Chem. Miner.* 46, 101–117. <https://doi.org/10.1007/s00269-018-0989-3>.
- Ulian, G., Tosoni, S., Valdrè, G., 2014. The compressional behaviour and the mechanical properties of talc  $[\text{Mg}_3\text{Si}_4\text{O}_{10}(\text{OH})_2]$ : a density functional theory investigation. *Phys. Chem. Miner.* 41, 639–650. <https://doi.org/10.1007/s00269-014-0677-x>.
- Weaver, J.S., 1976. Application of finite strain theory to non-cubic crystals. *J. Phys. Chem. Solids* 37, 711–718. [https://doi.org/10.1016/0022-3697\(76\)90009-3](https://doi.org/10.1016/0022-3697(76)90009-3).
- Weck, P.F., Kim, E., Jove-Colon, C.F., 2015. Relationship between crystal structure and thermo-mechanical properties of kaolinite clay: beyond standard density

- functional theory. *Dalton Trans.* 44, 12550–12560. <https://doi.org/10.1039/C5DT00590F>.
- Welch, M.D., Kleppe, A.K., Jeohcoat, A.P., 2004. Novel high-pressure behavior in chlorite: A synchrotron XRD study of clinocllore to 27 GPa. *Am. Mineral.* 89, 1337–1340. <https://doi.org/10.2138/am-2004-8-923>.
- Welch, M.D., Crichton, W.A., 2010. Pressure-induced transformations in kaolinite. *Am. Mineral.* 95, 651–654. <https://doi.org/10.2138/am.2010.3408>.
- Wenk, H.R., Bulakh, A., 2016. *Minerals: Their Constitution and Origin*. Cambridge University Press, Cambridge, UK.
- Wentzcovitch, R.M., Stixrude, L., 1997. Crystal chemistry of forsterite: A first-principles study. *Am. Mineral.* 82, 663–671. <https://doi.org/10.2138/am-1997-7-802>.
- Wibberley, C., 2007. Talc at fault. *Nature* 448, 756–757. <https://doi.org/10.1038/448756a>.
- Yang, D., Wang, W., Wu, W., 2017. Elasticity of superhydrous phase B at the mantle temperatures and pressures: Implications for 800 km discontinuity and water flow into the lower mantle. *J. Geophys. Res.: Solid Earth* 122, 5026–5037. <https://doi.org/10.1002/2017JB014319>.
- Yang, W., Li, Z.M., Shi, W., Xie, B.H., Yang, M.B., 2004. Review on auxetic materials. *J. Mater. Sci.* 39, 3269–3279. <https://doi.org/10.1023/B:JMSC.0000026928.93231.e0>.